



## 저작자표시-비영리-변경금지 2.0 대한민국

이용자는 아래의 조건을 따르는 경우에 한하여 자유롭게

- 이 저작물을 복제, 배포, 전송, 전시, 공연 및 방송할 수 있습니다.

다음과 같은 조건을 따라야 합니다:



저작자표시. 귀하는 원저작자를 표시하여야 합니다.



비영리. 귀하는 이 저작물을 영리 목적으로 이용할 수 없습니다.



변경금지. 귀하는 이 저작물을 개작, 변형 또는 가공할 수 없습니다.

- 귀하는, 이 저작물의 재이용이나 배포의 경우, 이 저작물에 적용된 이용허락조건을 명확하게 나타내어야 합니다.
- 저작권자로부터 별도의 허가를 받으면 이러한 조건들은 적용되지 않습니다.

저작권법에 따른 이용자의 권리는 위의 내용에 의하여 영향을 받지 않습니다.

이것은 [이용허락규약\(Legal Code\)](#)을 이해하기 쉽게 요약한 것입니다.

[Disclaimer](#)

# Nanosensor Research Based on Porous Silicon Photonic Crystals and Silicon Quantum Dots

광결정 다공성실리콘과 실리콘 양자점을 기초로한  
나노센서 연구

2017년 2월 24일

조선대학교 대학원

화학과

조 보 민

# Nanosensor Research Based on Porous Silicon Photonic Crystals and Silicon Quantum Dots

지도교수 손 홍 래

이 논문을 이학박사학위 신청 논문으로 제출함  
2016년 10월

조선대학교 대학원

화학과

조 보 민

## 조보민의 박사학위논문을 인준함

위원장	조선대학교	교수	<u>임 종 국</u>	(인)
위 원	조선대학교	교수	<u>이 범 규</u>	(인)
위 원	조선대학교	교수	<u>손 홍 래</u>	(인)
위 원	조선대학교	교수	<u>김 호 중</u>	(인)
위 원	세한대학교	교수	<u>고 영 춘</u>	(인)

2016년 12월

조선대학교 대학원

# TABLE OF CONTENTS

---

TABLE OF CONTENTS	I
LIST OF SYMBOLS AND ABBREVIATIONS	IV
LIST OF SCHEMES	VII
LIST OF FIGURES	VIII
ABSTRACT	XIII

## PART I. INTERFEROMETRIC NANOSENSORS BASED ON POROUS SILICON

### CHAPTER ONE

#### FABRICATION OF HUMAN IGG SENSORS BASED ON POROUS SILICON INTERFEROMETER CONTYANINING BRAGG STRUCTURES

1.1	Introduction.....	2
1.2	Experiments.....	4
1.2.1	Preparation of DBR and APSM Samples.....	4
1.2.2	Surface Derivatization of DBR PSi and APSM Samples.....	5
1.2.3	Instrumentation and Data Acquisition.....	6
1.3	Results and Discussion.....	7
1.3.1	Results for DBR PSi Samples.....	7
1.3.2	Results for ASPM Samples.....	11
1.4	Conclusions.....	19
1.5	References.....	20

### CHAPTER TWO

#### FABRICATION OF GRADIENT OPTICAL FILTER CONTAINING ANISOTROPIC BRAGG NANOSTRUCTURE AND MULTI-ENCODED RUGATE POROUS SILICON/POLYMER COMPOSITE

23

<b>2.1</b>	<b>Introduction.....</b>	<b>23</b>
<b>2.2</b>	<b>Experiments.....</b>	<b>25</b>
2.2.1	Preparation of MRPS and Anisotropic DBR PSi Films.....	25
2.2.2	Preparation of MRPS and Anisotropic DBR PSi Composite Films.....	26
2.2.3	Preparation of Gas Samples.....	27
2.2.4	Instruments and Data Acquisitions.....	27
<b>2.3</b>	<b>Results and Discussion.....</b>	<b>28</b>
2.3.1	Results for MRPS Samples.....	28
2.3.2	Results for Anisotropic DBR PSi Samples.....	33
<b>2.4</b>	<b>Conclusions.....</b>	<b>38</b>
<b>2.5</b>	<b>References.....</b>	<b>39</b>

## CHAPTER THREE

### DETECTION OF ORGANIC VAPORS BASED ON PHOTOLUMINESCENT BRAGG-REFLECTIVE PRORUS SILICON INTERFEROMETER 42

<b>3.1</b>	<b>Introduction.....</b>	<b>42</b>
<b>3.2</b>	<b>Experiments.....</b>	<b>43</b>
3.2.1	Preparation of PBR PS.....	43
3.2.2	Instruments and Data Acquisitions.....	43
<b>3.3</b>	<b>Results and Discussion.....</b>	<b>45</b>
<b>3.4</b>	<b>Conclusions.....</b>	<b>53</b>
<b>3.5</b>	<b>References.....</b>	<b>54</b>

## PART II. FLUORESCENT NANOSENSORS BASED ON SILICON QUANTUM DOTS

### CHAPTER ONE

FABRICATION AND CHARACTERIZATION OF PHOTOLUMINESCENT SILICON NANOPARTICLES FOR DRUG DELIVERY APPLICATIONS		57
1.1	Introduction.....	57
1.2	Experiments.....	58
1.2.1	Preparation of Photoluminescent PSi.....	58
1.2.2	Surface Oxidation of Photoluminescent PSi.....	58
1.2.3	Preparation of CPT-Derivatized Silicon Nanoparticles.....	58
1.2.4	Instrumentation and Data Acquisition.....	59
1.3	Results and Discussion.....	60
1.4	Conclusions.....	66
1.5	References.....	67

### CHAPTER TWO

SILICON QUANTUM DOT SENSORS FOR AN EXPLOSIVE TAGGANT, 2,3-DIMETHYL-2,3-DINITROBUTANE (DMNB)		69
2.1	Introduction.....	69
2.2	Experiments.....	70
2.3	Results and Discussion.....	71
2.4	Conclusions.....	79
2.5	References.....	80

<b>APPENDICES</b>	84
<b>APPENDIX : CURRICULUM VITAE</b>	85



## LIST OF SYMBOLS AND ABBREVIATIONS

---

$\text{\AA}$	Angstrom
$\beta$	Beta
cm	Centimeter
$^{\circ}\text{C}$	Celsius temperature scale
$\text{m}^3$	Cubic Meter
d	Diameter
$\delta$	Delta
$\epsilon$	Epsilon
$\lambda_{\text{em}}$	Emission Wavelength
fg	Femtogram
<i>d</i>	Film thickness
g	Gram
$\text{h}^+$	Hole
h	Hour
kJ	Kilojoule
$\lambda$	lambda
L	Liter
m	Mass
M	Molarity
$\mu\text{m}$	Micrometer
mg	Milligram
mA	Milliampere
mmol	Millimole
mL	Milliliter
$\lambda_{\text{max}}$	Maximum Wavelength
$\mu$	Mu
$\mu\text{M}$	Micromolarity
$\text{M}_w$	Molecular Weight
$\mu\text{g}$	Microgram

<b>MHz</b>	MegaHertz
<b>ν</b>	Nu
<b>nm</b>	Nanometer
<b>Ω</b>	Ohm
<b>π</b>	Pi
<b>%</b>	Percent
<b>n</b>	Refractive Index
<b>σ</b>	Sigma
<b>T</b>	Thickness
<b>t</b>	Time
<b>vs</b>	Versus
<b>V</b>	Volume
<b>W</b>	Watt
<b>A.U.</b>	Arbitrary Units
<b>Al</b>	Aluminium
<b>AIE</b>	Aggregation-Induced Emission
<b>BET</b>	Brunauer-Emmett-Teller
<b>BuLi</b>	Butyllithium
<b>Cu</b>	Copper
<b>CWA</b>	Chemical Warfare Agents
<b>c-Si</b>	Crystalline Silicon
<b>CCD</b>	Charge-Coupled Detector
<b>CdSe</b>	Cadmium Selenide
<b>DCP</b>	Diethyl Chlorophosphate
<b>DFP</b>	Diisopropyl Phosphonate
<b>DEEP</b>	Diethyl Ethylphosphonate
<b>DMMP</b>	Dimethyl Methylphosphonate
<b>DNA</b>	Deoxyribonucleic Acid
<b>DMF</b>	Dimethyl Formaldehyde
<b>DNT</b>	Dinitrotoluene
<b>EL</b>	Electroluminescence
<b>EDS</b>	Energy Dispersive X-ray Spectrometry

<b>FIPOS</b>	Full Isolated Porous Oxidized Silicon
<b>FWHM</b>	Full-Width at Half-Maximum
<b>F-P</b>	Fabry-Pérot
<b>FT-IR</b>	Fourier Transform Infrared Spectroscopy
<b>HOMO</b>	Highest Occupied Molecular Orbital
<b>HF</b>	Hydrofluoric Acid
<b>IC</b>	Integrated Circuit
<b>InP</b>	Indium phosphate
<b>InAs</b>	Indium Arsenide
<b>LCT</b>	Lethal Concentration
<b>LED</b>	Light Emitting Diode
<b>LUMO</b>	Lowest Unoccupied Molecular Orbital
<b>LiAlH<sub>4</sub></b>	Lithium Aluminum Hydride
<b>MEMS</b>	Micro Electro Mechanical Systems
<b>MALDI</b>	Matrix-Assisted Laser Desorption Ionization
<b>Mg<sub>2</sub>Si</b>	Magnesium Silicide
<b>NaOH</b>	Sodium Hydroxide
<b>NA</b>	Nerve Agents
<b>NA</b>	Nanoaggregates
<b>NP</b>	Nanoparticle
<b>NMR</b>	Nuclear Magnetic Resonance
<b>OSHA</b>	Occupational Safety and Health Administration
<b>PSi</b>	Porous Silicon
<b>Pt</b>	Platinum
<b>PL</b>	Photoluminescence
<b>PA</b>	Picric Acid
<b>PBS</b>	Phosphate Buffer Solution
<b>PSA</b>	Particle Size Analyzer
<b>ppm</b>	Part Per Million
<b>ppb</b>	Part Per Billion
<b>ppt</b>	Part Per Trillion
<b>pmol</b>	Picomole
<b>R.T.</b>	Room Temperature
<b>SAED</b>	Selected Area Electron Diffraction
<b>Si</b>	Silicon
<b>SiO<sub>2</sub></b>	Silicon Dioxide
<b>sec</b>	Second

<b>SAW</b>	Surface Acoustic Wave
<b>SOI</b>	Silicon-On-Insulator
<b>S-V Eqn</b>	Stern-Volmer Equation
<b>SWNT</b>	Single-walled Nanotube
<b>TLC</b>	Thin-Layer Chromatography
<b>TNT</b>	Trinitrotoluene
<b>TMS</b>	Tetramethylsilane
<b>THF</b>	Tetrahydrofuran
<b>TMEDA</b>	Tetramethyl Ethylene Diamine
<b>TEP</b>	Triethylphosphate
<b>TEOS</b>	Tetraethyl orthosilicate
<b>TOPO</b>	Tri- <i>n</i> -octylphosphineoxide
<b>UV</b>	Ultraviolet
<b>UV-Vis</b>	Ultraviolet-Visible

## LIST OF SCHEMES

---

- Scheme 1.1      Schematic process for surface modification of DBR PSi with biotin.
- Scheme 1.2      Schematic process for the detection of Human IgG.

## LIST OF FIGURES

---

### PART I. INTERFEROMETRIC NANOSENSORS BASED ON POROUS SILICON

- Figure 1.1 Surface and cross-sectional SEM images of DBR PSi
- Figure 1.2 Diffuse reflectance FT-IR spectra of (A) freshly etched DBR PSi, (B) thermally oxidized DBR PSi, (C) amine-functionalized DBR PSi, and (D) biotin-functionalized DBR PSi.
- Figure 1.4 Schematic diagram of the      Figure 3.2 Illustration (left) and photograph etch cell with Pt counter electrode      (right) of APSM sample for the generation of APSM.
- Figure 1.5 Illustration (left) and (right) of APSM sample.
- Figure 1.6 Surface and cross-sectional SEM images of spot 1 in APSM.
- Figure 1.7 Reflection spectra measured at each spot.
- Figure 1.8 Schematic diagrams for the surface functionalization of APSM and the detection of Human Ig G with APSM chip.
- Figure 1.9 FT-IR spectra of (A) as-prepared, (B) thermally oxidized, (C) amine-derivatized, and (D) biotin-derivatized APSM.
- Figure 1.10 Reflection spectra of spot 1 in (A) oxidized, (B) aminederivatized, (C) biotin-derivatized, (D) PBS-rinsed, (E) streptavidinflushed, (F) biotinylated protein A-flushed, (G) human Ig G-flushed APSM.
- Figure 1.11 Changes of reflection wavelengths according to the step-bystep

addition of proteins in APSM.

Figure 1.12 Differential plots for showing the specificity for the detection of human Ig G. at each spot in APSM.

Figure 2.1 Schematic diagram for the fabrication of MRPS film.

Figure 2.2 Surface and cross-sectional SEM images of MRPS/polymer composite film.

Figure 2.3 Reflection resonance spectra under exposure to different analytes such as hexane and methanol.

Figure 2.4 Real time responses of intensities at the fixed wavelength of reflection maxima under exposure to hexane (top) and methanol (bottom) vapors.

Figure 2.5 First derivatives for the capillary condensation of hexane vapor.

Figure 2.6 3D plot showing the relationship between the wavelength shift of the reflection bands ( $\Delta \lambda$ ,  $\Delta I/\Delta T$ , and intensity change for methanol and hexane vapors.

Figure 2.7 Schematic diagram of the etch cell with plate Pt electrode for the formation of anisotropic DBR PSi.

Figure 2.8 Surface (left) and cross-section (right) images of anisotropic DBR PSi measured at the lateral distance from a point closest to the Pt counter electrode to the silicon surface: [A] at 0 mm, [B] at 30 mm, [C] at 45 mm, and [D] at 60 mm.

Figure 2.9 Schematic diagram for the generation of anisotropic DBR PSi composite film and photographs of free-standing anisotropic

DBR PSi film (left), oxidized anisotropic DBR PSi film (middle), and anisotropic DBR PSi composite film (right).

Figure 2.10 Reflection spectra of anisotropic DBR PSi composite film as a function of lateral distance displayed reflection maxima of 650, 632, 612, 590, 574, 551, 534 nm at lateral of 0, 15, 30, 45, 60, 75, 90 mm, respectively.

Figure 2.11 Reflection wavelength maximum as a function of distance on the anisotropic DBR PSi composite film.

Figure 3.1 Photographs of PBR PS under white light (left) and black light (right). Dark area at the red luminescent region is due to the quenching of the PL after exposure to water vapor.

Figure 3.2 Surface (top) and cross-section (bottom) SEM images of PBR PS.

Figure 3.3 Reflectivity (green line) and PL (red line) spectra of PBR PS.

Figure 3.4 FT-IR spectrum of PBR PS.

Figure 3.5 Reflection spectra of fresh PBR PS(blue,  $\lambda = 761$  nm) and PBR PS under a flux of benzene (black,  $\lambda = 788$  nm,  $\Delta\lambda = 27$  nm), methanol (green,  $\lambda = 796$  nm,  $\Delta\lambda = 35$  nm), and acetone (red,  $\lambda = 809$  nm,  $\Delta\lambda = 48$  nm).

PL spectra of PBR PS under a flux of acetone (black),

Figure 3.6 methanol (green), and benzene (red).

Figure 3.7 A plot for the relationship between the different vapor pressures of three analytes and the change of Bragg reflection wavelength (left). Stern-Volmer plots for three different analytes at various vapor pressures (right).

Figure 3.8 3D plot showing the relationship between the wavelength shift of the reflection peak and quenching PL as a function of different vapor pressures of three analytes such as acetone (red), methanol (green), and benzene (blue). photoluminescence (%).

## **Part II. FLUORESCENT NANOSENSORS BASED ON SILICON QUANTUM DOTS**

Figure 1.1 Schematic diagram for the preparation of CPT-derivatized Si Nps.

Figure 1.2 Chemical reactions for the surface derivatization of Si NPs with CPT.

Figure 1.3 FT-IR spectra of fresh PSi sample (a), surface-oxidized PSi sample (b), and CPT-derivatized PSi sample ©.

Figure 1.4 CPT release in buffer solutions as a function of time, measured by using an absorption band at 369 nm.

Figure 1.5 FE-SEM images of CPT-derivatized Si NPs.

Figure 1.6 UV-vis absorption (dashed line) and PL (solid line) spectra for CPT (red), Si NPs (blue), and CPT-derivatized Si NPs (black).

Figure 1.7 Plot for the stability of CPT-derivatized Si NPs in PBS buffer solution.

Figure 1.8 PL spectra during the release of CPT from Si NPs.

Figure 2.1 UV absorption band and PL spectra of blue ( $\lambda_{\text{max}} = 460 \text{ nm}$ ) and green ( $\lambda_{\text{max}} = 520 \text{ nm}$ ) luminescent Si QDs, showing blue and green PL under a UV light lamp (inset).



Figure 2.2 HRTEM image (a), a SAED pattern (b), and fast Fourier transform image (c) of Si QDs.

Figure 2.3 PL quenching spectra of Si QDs recorded upon every addition of  $1.11 \times 10^{-6}$ ,  $2.18 \times 10^{-6}$  M,  $3.21 \times 10^{-6}$  M,  $4.20 \times 10^{-6}$  M, and  $5.16 \times 10^{-6}$  M of DMNB at each  $\lambda_{\text{max}} = 460$  nm (blue) and  $\lambda_{\text{max}} = 520$  nm (green) of Si QDs.

Figure 2.4 The Stern-Volmer plots for quenching efficiency of the blue and green photoluminescent Si QDs with the introduction of DMNB.

Figure 2.5 Fluorescence decays of blue luminescent Si QDs for different concentrations of DMNB; the plots of fluorescence lifetime ( $\tau_0/\tau$ ), shown in the inset, are independent of the added DNMB.

Figure 2.6 Quenching of photoluminescence spectra of the blue (blue) and green (green) luminescent CdSe QDs with addition of  $1.11 \times 10^{-6}$  M,  $2.18 \times 10^{-6}$  M,  $3.21 \times 10^{-6}$  M,  $4.20 \times 10^{-6}$  M, and  $5.16 \times 10^{-6}$  M of DMNB.

Figure 2.7 Qualitative band diagram of Si QDs (left) and CdSe QDs (right) illustrated for sensitivity to DMNB. CB band edge level for Si QDs was optimized at the 6-31G\* level, with the final energy also calculated at the 6-31G\* level. LUMO of DMNB was determined by theoretical calculations at the B3LYP/6-31G\* level of theory. CB band edge value for CdSe QD was directly taken from research by Querner et al.

## 초 록

### 광결정 다공성실리콘과 실리콘 양자점을 기초로한 나노센서 연구

박사과정 : 조 보 민

지도교수 : 손 홍 래

조선대학교 화학과

최근 수 십 년간 전기·전자 및 금속·반도체기술이 눈부신 발전을 이룩하였다면 21세기 현대과학에서는 새로운 형태나 특성을 연구하는 영역으로 나노과학 및 나노기술이 급속히 발전하고 있다. 현대 화학이 여러 분야로 세분화되고, 전문화되어지면서 광화학 이나 나노화학 에 대한 관심도가 매우 높아지고 있다. 특히, 나노소재를 이용한 분야가 매우 빠른 속도로 발전하고 있다. 나노과학은 나노소재의 합성 및 응용분야로 분류된다. “나노센서”는 나노과학의 한 응용분야로서 분자 수준의 조작이 가능한 분자센서의 집적화 또는 나노소재 나 나노구조물 의 특성을 이용한 센서를 의미한다. 나노소재로는 나노다공질재료 , 금속 및 반도체소재의 나노와이어, 나노입자, 나노튜브 등이 있으며 기질을 인지 또는 감지할 수 있는 나노소재로부터 장치를 만들었을 경우 나노센서라 일컫는다.

최근 나노센서 또는 나노바이오센서 등에 대한 관심이 나노과학의 한 분야로서 지대한 관심의 대상이 되고 있는데 그 이유는 고감도, 초소형의 센서 구현을 통해서 생명현상인 분자 간의 상호작용을 나노크기의 수준에서 탐구하려는 학문적인 관심과 함께 응용적인 측면에서 보건의

료, 식품, 환경, 국방 등의 다양한 분야에서 활용되는 센서를 개발하기 위한 실질적인 중요성 때문에 학계와 연구소, 그리고 산업체에서 활발히 연구되고 있다. 특히 나노 신소재 개발 분야는 기초과학에서부터 첨단과학까지의 융합학제 간 학문 분야로 미래기술의 선점 및 국가경쟁력 확보에 있어서 우위를 차지하는데 중요한 역할을 할 것으로 기대된다.

따라서 본 연구논문의 주제는 나노화학 및 바이오센서 개발의 일환으로 반도체 실리콘 재료를 이용하여 화학 및 생물학적 센서재료 및 폭발물탐지의 개발을 목표로 한다. 연구논문의 구성은 전반부에는 실리콘 웨이퍼를 전기화학적 식각을 통하여 얻어진 다공성 실리콘을 이용하여 광학적인 특성을 조사후 화학센서 재료로 사용하였고, 후반부에는 형광성을 갖는 실리콘 양자점에 대한 합성방법과 광학적 특성을 조사하였고, 광 발광성 실리콘양자점을 통하여 폭발물의 구성성분인 니트로방향족 화합물을 탐지하는 센서재료와 인체에 적합한 실리콘양자점에 특성을 살려 생물학센서로 응용 연구하였다.

# **Part I.**

# **INTERFEROMETRIC**

# **NANOSENSORS BASED**

# **ON POROUS SILICON**

## Chapter One

# Fabrication of Human IgG Sensors Based on Porous Silicon Interferometer Containing Bragg Structures

### 1.1 Introduction

Recently, the nanostructured porous silicon (PSi) has been received a great interest in optoelectronic devices.<sup>1</sup> The PSi has a high surface area, which has shown to be useful for many applications, such as chemical and biological sensors,[2-4] switching devices,[4] implantable biomaterials,[5] drug delivery,[6] and in high-throughput screening.[7] The direction of pores and pore diameters in PSi depend on surface orientation, doping level and type, temperature, the current density, and the composition of the etching solution.[8] The most important performance parameters of optical biosensors are reflective index (n) and signal intensity.[9,10] Photonic crystals such as distributed Bragg reflectors (DBR) have been extensively studied in recent years because of their unique optical properties and the possibility of modulating the spectral resonance of optical spectrum. DBR PSi prepared by applying a computer generated pseudo-square current waveform results two distinct indices and exhibits photonic structure of Bragg filters.[11,12] The mth order of the Bragg peak is given by  $m\lambda_{\text{Bragg}} = 2(d_1n_1 + d_2n_2)$ . DBR PSi exhibits unique optical properties providing the reflection of a specific wavelength in the optical reflectivity spectrum. For applications in biosensors,

label-free biosensors would be important due to the advantage of easy sample preparation.[13] The main transduction methods for label-free biosensors are optical interferometers,[14] evanescent wave devices,[15] grating couplers,[16] and surface plasmon methods.[17] Biosensor based on P*Si* interferometer has a great advantage due to a large surface area matrix for immobilization of a variety of biomolecules such as enzymes,[18] protein,[19] and DNA fragments.[20] Recently, the double-layers of P*Si* can also be used as the transducer of biomolecular interaction in biosensor application[.21] In the present work, a simply modified biosensor for the detection of human immunoglobulinG (IgG) based on protein A-modified DBR P*Si* and APSM interferometer is reported. The fabrication, optical characterization, and surface derivatization of DBR P*Si* and APSM are investigated.

## 1.2 Experiments

### 1.2.1 Preparation of DBR and APSM Samples

The DBR PSi was prepared by an electrochemical etching of Si wafer (boron doped, polished on the <100> face, resistivity of  $0.8 \sim 1.2 \text{ m}\Omega \cdot \text{cm}$ , Siltronix, Inc.). The etching solution consisted of a 1:3 (v/v) mixture of absolute ethanol (ACS reagent, Aldrich Chemicals) and aqueous 48% hydrofluoric acid (ACS reagent, Aldrich Chemicals). Galvanostatic etching was carried out in a Teflon cell by using a two-electrode configuration with a Pt mesh counter electrode. DBR PSi was prepared by using a periodic pseudo-square wave current between  $350 \text{ mA} \cdot \text{cm}^{-2}$  for 1 s and  $100 \text{ mA} \cdot \text{cm}^{-2}$  for 5 s. The anodization current was supplied by Keithley 2420 high-precision constant current source controlled by a computer allow the formation of PSi. and Spot array of APSM samples were prepared by an electrochemical etching of the heavily doped p-type Si <100> substrate (boron doped, polished on the (100) face, resistivity of  $0.8\text{-}1.2 \text{ m}\Omega \cdot \text{cm}$ , Siltronix, Inc.). The etching solution consists of a 1:3 by volume mixture of absolute ethanol (ACS reagent, Aldrich Chemicals) and aqueous 48% HF (Aldrich Chemicals). Teflon template containing 9 holes, whose radius and interval distances were 2 mm, was placed on the top of silicon wafer. Etching was carried out in a Teflon cell by using a two-electrode configuration with a Pt wire counter electrode placed at the end of etching cell to have the structural anisotropies. APSM sample having Bragg structure was prepared by using a periodic pseudo-square wave current between  $41.5 \text{ mA} \cdot \text{cm}^{-2}$  for 0.5 s and  $0.8 \text{ mA} \cdot \text{cm}^{-2}$  for 4 s with 50 repeats. To prevent the photo-generation of carriers, the anodization was performed in the dark.

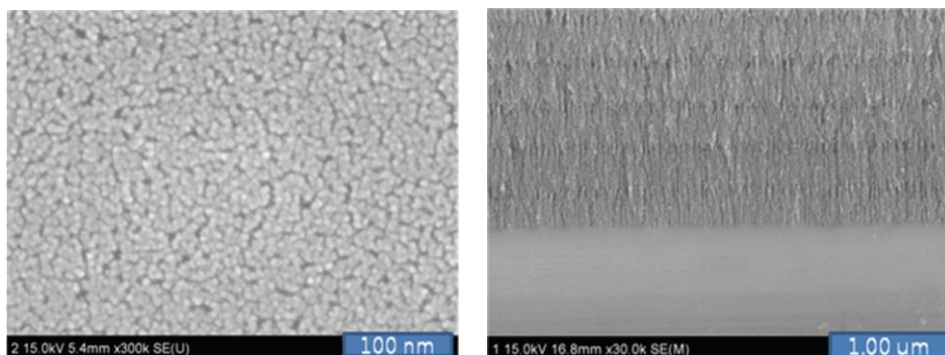


Figure. 1.1 Surface and cross-sectional SEM images of DBR PSi.

All DBR and ASPM PSi samples were then rinsed several times with ethanol and dried under argon atmosphere.

### 1.2.2 Surface Derivatization of DBR PSi and ASPM Samples

Thermal oxidized DBR and ASPM PSi samples were obtained by heat treatment in a furnace (Thermolyne F6270-26 furnace equipped with controller) using the following parameters: initial ramp rate, °C/min to 300 °C, hold time, 3 h and passive cooling to ambient temperature.

For the functionalization of oxidized DBR and ASPM PSi, the oxidized DBR and ASPM PSi sample and 5 mL of (3-aminopropyl) trimethoxysilane (99%, Aldrich Chemicals) were placed in Schlenk flask and refluxed for 12 hrs in a dry argon atmosphere. After functionalization with amine group, the DBR and ASPM PSi sample was rinsed successively with methylene chloride, acetone, and ethanol and subsequently dried under a stream of nitrogen.

For surface modification of biotin-derivatized DBR and ASPM PSi sample, 10 mg of biotinamidohexanppyl-6-amino hexanoic acid N-hydroxy-succinimide ester (95% Aldrich Chemicals) was dissolved in 20 mL of



dimethylformamide. The mixture solution was stirred vigorously for 10 min. The biotin-derivatized DBR and APSM PSi chip, 1-(3-(dimethylamino) propyl)-3-ethylcarbodiimidehydro-chloride (EDC, 20 mg, 0.1 mmol), and triethylamine (TEA, 0.9 mL, 6 mmol) were added to the mixture solution. The reaction mixture was allowed to stir at room temperature for overnight. After removal of the solution, samples were rinsed by ethanol, methylene chloride, and acetone, dried under a reduced pressure, and stored in nitrogen atmosphere prior to use.

### 1.2.3 Instrumentation and Data Acquisition

Interferometric reflectance spectra of DBR and APSM PSi were recorded by using an Ocean Optics S2000 spectrometer fitted with a bifurcated fiber optic probe. A tungsten light source was focused onto the center of DBR and APSM PSi surface with a spot size of approximately 1~2 mm. Spectra were recorded with a CCD detector in the wavelength range 400~1200 nm. The illumination of the surface as well as the detection of the reflected light was performed along an axis coincident with the surface normal. FT-IR instrument in the diffuse reflectance mode (Spectra-Tech diffuse reflectance attachment), with diffuse reflectance absorption spectra are reported in absorbance units. The morphology of DBR and APSM PSi film was observed with cold field emission scanning electron microscope (FE-SEM, S-4700, Hitachi).

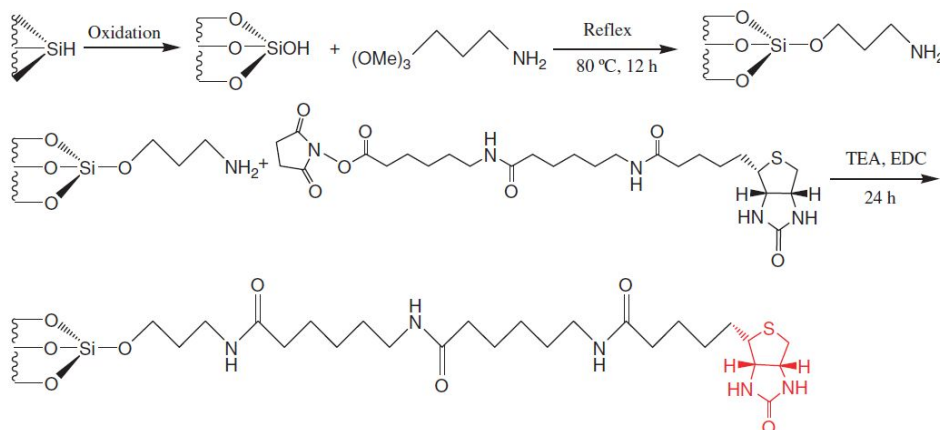
## 1.3 Results and Discussion

### 1.3.1 Results for DBR PSi Samples

A DBR PSi exhibits a high reflectivity band with the Bragg wavelength,  $\lambda_{\text{Bragg}}$ , depending on the thickness of the layers ( $d_1$ ,  $d_2$ ) and the corresponding refractive indices ( $n_1$ ,  $n_2$ ). The  $m$ th order of the Bragg peak is given by

$$m \lambda_{\text{Bragg}} = 2(d_1 n_1 + d_2 n_2) \quad (1)$$

Typical etch parameters for the DBR PSi structure involve using a periodic square-wave current between low and high current densities. The pore shape, pore size, and orientation of porous silicon layers depend on the surface orientation and doping level and type, temperature, the current density, and the composition of the etching solution. In this work, the applied current densities for the fabrication of DBR PSi was varied between 100 and 350  $\text{mA} \cdot \text{cm}^{-2}$ .



Scheme. 1.1 Schematic process for surface modification of DBR PSi with biotin.

The surface and cross sectional morphology of DBR PSi were obtained with cold FE-SEM and shown in Figure 1.1 The cross-sectional images of DBR PSi displayed that the DBR PSi has a depth of about 20 microns. A repeating etching process results in two distinct refractive indices. The chemistry of functionalization was outlined in Scheme 1. The thermal oxidation of PSi at 300 °C converted the hydride-terminated surface into hydroxyl terminated PSi. Condensation of the Si.OH surface of PSi with (3-aminopropyl)trimethoxysilane generated a surface-bound amine group. The subsequent reaction with biotinamidohexanppyl-6-amino hexanoic acid N-hydroxysuccinimide ester, EDC, and TEA led to the desired biotin-functionalized DBR PSi which was used in the streptavidin-binding studies.

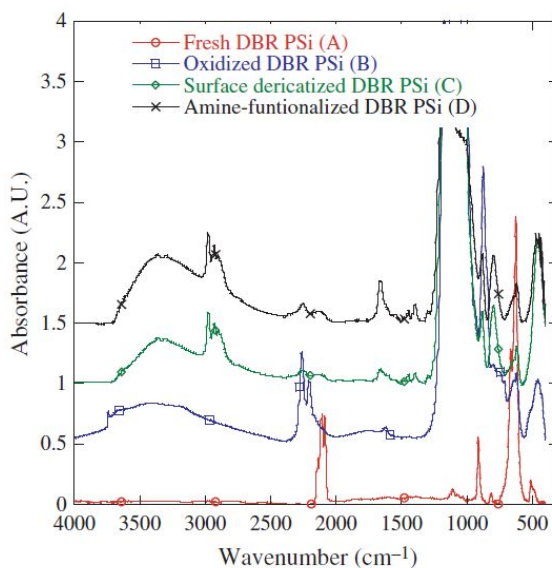
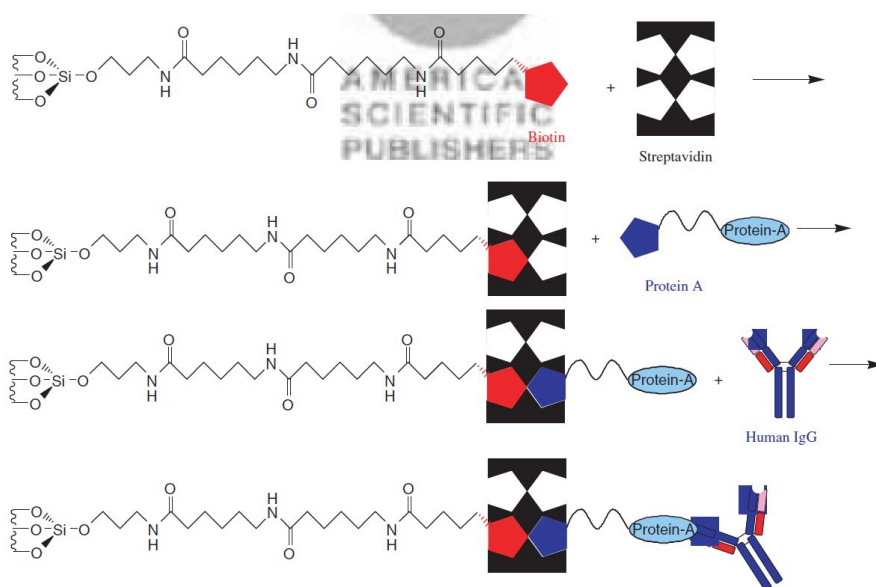


Figure. 1.2 Diffuse reflectance FT-IR spectra of (A) freshly etched DBR PSi, (B) thermally oxidized DBR PSi, (C) amine-functionalized DBR PSi, and (D) biotin-functionalized DBR PSi.

Diffuse reflectance FT-IR spectroscopy was used to monitor the oxidation and functionalization reaction of DBR PSi. Figure 1.2 showed that the FTIR spectrum of freshly etched DBR PSi displayed absorptions characteristic of surface SiH, SiH<sub>2</sub>, and SiH<sub>3</sub> species at 2086, 2115, and 2138 cm<sup>-1</sup>, respectively, with no detectable surface oxide absorptions. Thermal oxidation of DBR PSi resulted in a significant loss of intensity of the  $\nu_{(\text{Si-H})}$  modes, but vibrational bands due to oxygen back-bonded silicon hydride,  $\nu_{(\text{OSi-H})}$  and  $\delta_{(\text{OSi-H})}$  modes, grew in at 2209 and 2263 cm<sup>-1</sup>. Multiple silicon oxide species, Si-O-Si, displayed a strong broad silicon oxide stretching mode at 1100 cm<sup>-1</sup>. Amine-functionalized DBR PSi displayed additional band characteristics of the amine band of  $\nu_{(\text{N-H})}$  at 3361 cm<sup>-1</sup> and the aliphatic



Scheme 1.2 Schematic process for the detection of Human IgG.

$\nu_{(\text{C-H})}$  stretching bands at 2898, 2931, and 2975 cm<sup>-1</sup>. Biotin-functionalized

DBR PSi displayed additional band characteristics of the amide band of  $\nu_{(\text{CON})}$  at  $1662\text{ cm}^{-1}$ . The biotin-functionalized DBR PSi was placed in the flow cell. Aqueous PBS buffer solution was flushed to perform an initial measurement of reflectivity. The chemistry of binding event of biomolecules was outlined in Scheme 2. The surface was rinsed thoroughly with PBS buffer solution to ensure covalent attachment to the surface and to check stability of the reflectivity measurement. The cell was then flushed with a constant flow of  $0.8\text{ mL/min}$  of PBS buffer solution containing protein ( $20\text{ }\mu\text{M}$  streptavidin, biotinylated protein A, and human IgG) which coupled to the biotin-modified DBR PSi surface.

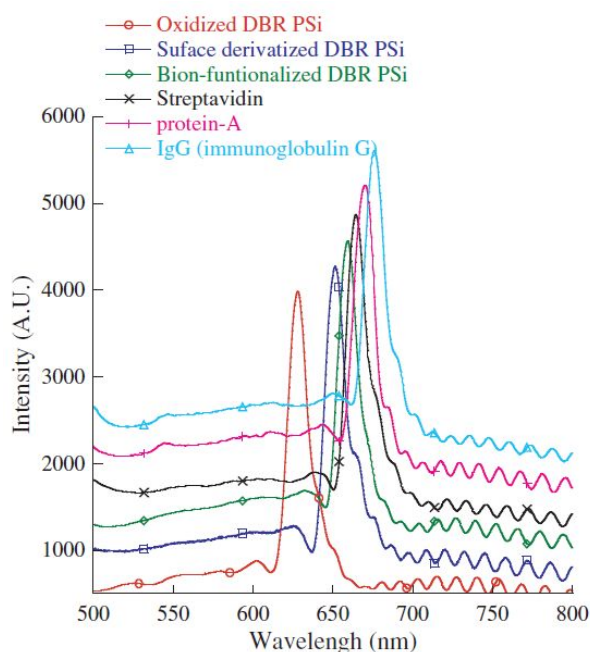


Figure. 1.3 Change of optical reflectivity in the reflection spectra depending on the surface modification of DBR PSi.

Figure 1.3 showed the change of reflectivity in the reflection spectrum depending on the surface modification of DBR PSi. Oxidized DBR PSi displayed a very sharp line at 628 nm with sidelobes around the reflectance peak in the optical reflectivity spectrum. The spectral bands of DBR PSi had a full-width at half maximum (FWHM) of about 18 nm. The amine-functionalized DBR PSi resulted in the reflectivity at 651 nm shifted to longer wavelengths by 23 nm due to the increase of refractive indices upon introduction of the amine group into the pores of DBR PSi. The subsequent introduction of biotin derivatives to the amine-functionalized DBR PSi resulted in the reflectivity at 657 nm shifted to longer wavelengths by 6 nm, due to the increase of additional refractive indices. For binding studies, the exposure of 20  $\mu$ M streptavidin to the biotin-functionalized DBR PSi resulted in an increase of the reflection wavelength in the reflectivity spectrum by 7 nm, indicative of a change in refractive indices induced by binding of the streptavidin into the biotin-derivatized DBR PSi. The subsequent introduction of 20  $\mu$ M biotinylated protein A resulted in the reflectivity shifted to longer wavelengths by 6 nm, indicative of a change in refractive indices induced by binding of streptavidin and biotinylated protein A. Finally the addition of 20  $\mu$ M human IgG resulted in the reflectivity shifted to further longer wavelengths by 6 nm, indicative of binding of protein A and human IgG.

### 1.3.2 Results for ASPM Samples

APSM sample shown in Figure 1.4 was generated by an electrochemical etching of silicon wafer with an asymmetric etching configuration. Diagram (left) and photograph (right) of APSM sample are shown in Figure 2. Size of each spot in diameter and inter-spot distance were 2 mm. Spot 1 in Figure 2 represented the first spot generated under the Pt counter electrode. Red

reflection color from the first spot gradually changed to green reflection color as the lateral distance increased. Surface and cross-sectional images of first spot in APSM obtained by using a cold field emission scanning electron microscope were shown in Figure 3. The surface SEM images of APSM indicated that the pore size of spot porous silicon gradually decreased as the lateral distance increased.[12] Cross-sectional SEM image of PSi displayed two discrete porous layers.

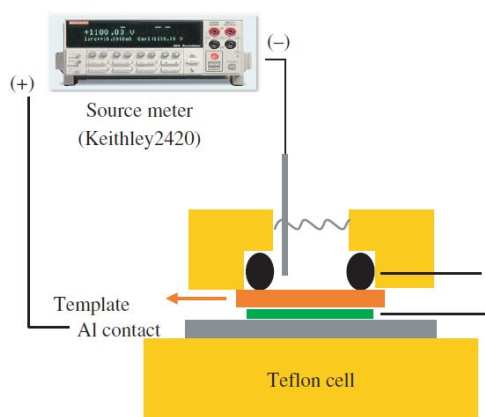


Figure 1.4 Schematic diagram of the photograph etch cell with Pt counter electrode for the generation of APSM.

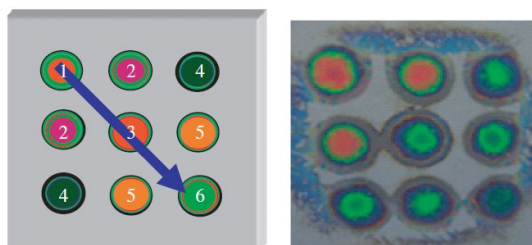


Figure 1.5 Illustration (left) and (right) of APSM sample.

Reflection resonances in the optical reflective spectra for each spot were

shown in Figure 1.7 The reflection spectra of APSM indicated that the reflection wavelength gradually shifted to shorter wavelength as the lateral distance increased. The chemistry of functionalization was outlined in Figure 1.8 The thermal oxidation of APSM converted the hydride-terminated surface into hydroxyl terminated surface. Condensation of the Si-OH surface with (3-aminopropyl) trimethoxysilane generated a surface-bound amino group. The subsequent reaction with biotin derivatives led to the desired biotin-functionalized surface. FT-IR spectroscopy was used to monitor the oxidation and functionalization of APSM sample. Figure 1.9(A)

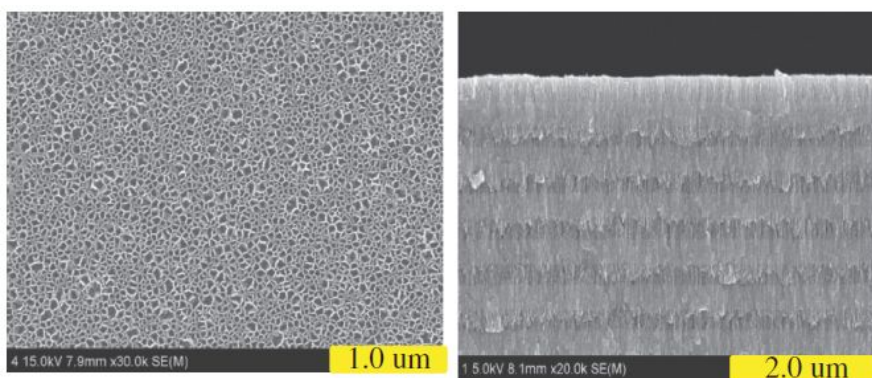


Figure 1.6 Surface and cross-sectional SEM images of spot 1 in APSM.

Spot 1 was measured at the lateral distance from a point closest to the Pt electrode showed that the FT-IR spectrum as-prepared APSM displayed a characteristic broad band centered at  $2119\text{ cm}^{-1}$  for the  $\nu(\text{Si-H})$  stretching vibration. The oxidized APSM shown in Figure 6(B) displayed a significant loss of intensity of the  $\nu(\text{Si-H})$  modes, but vibrational bands of oxygen-back-bonded silicon hydride,  $\nu(\text{OSi-H})$  modes, grew at  $2200\text{--}2250\text{ cm}^{-1}$ . Silicon oxide species, Si-O-Si, displayed a strong, very broad absorption band



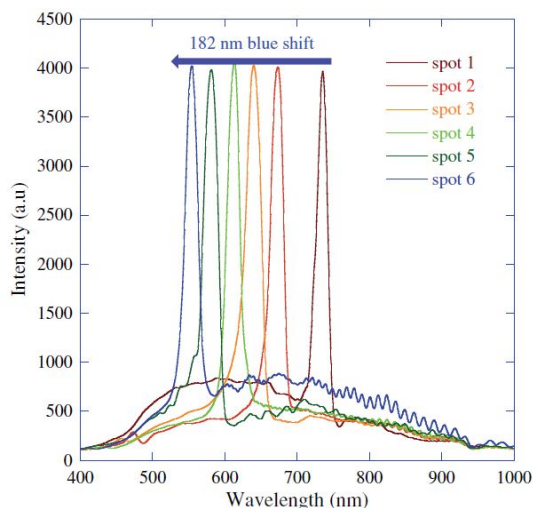


Figure 1.7 Reflection spectra measured at each spot.

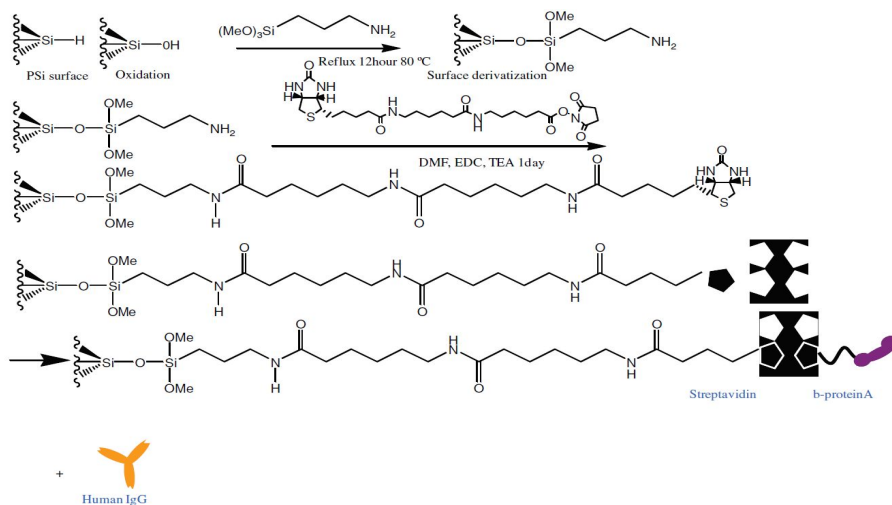


Figure 1.8 Schematic diagrams for the surface functionalization of APSM and the detection of Human Ig G with APSM chip.

at 1000-1200  $\text{cm}^{-1}$ . Amine-derivatized APSM shown in Figure 6(C) displayed  $\delta(\text{N-H})$  at 1575  $\text{cm}^{-1}$  and the aliphatic  $\nu(\text{C-H})$  stretching bands at around 2952  $\text{cm}^{-1}$ . The band shown in Figure 2(D) at 1652  $\text{cm}^{-1}$  was assigned to the carbonyl stretching vibration of the biotin head group.

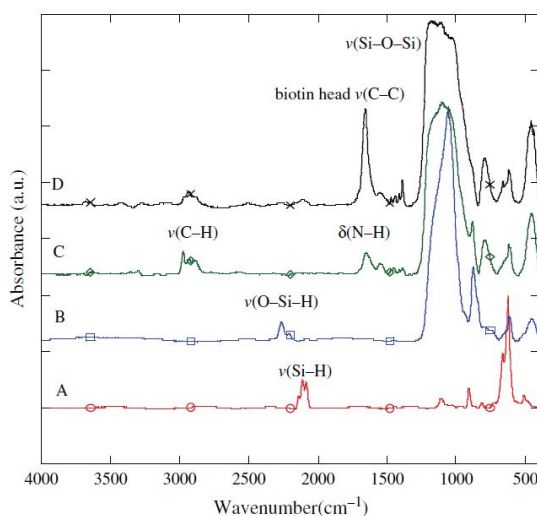


Figure 1.9 FT-IR spectra of (A) as-prepared, (B) thermally oxidized, (C) amine-derivatized, and (D) biotin-derivatized APSM.

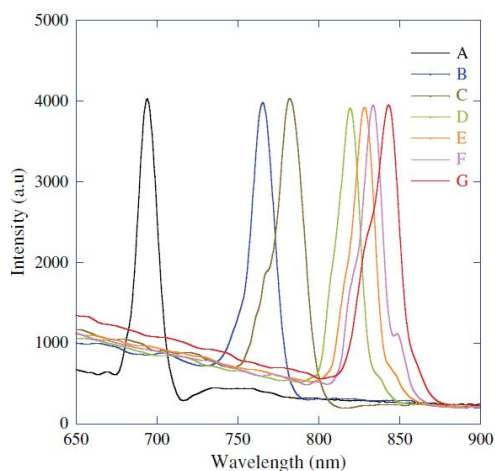


Figure 1.10 Reflection spectra of spot 1 in (A) oxidized, (B) aminated, (C) biotin-derivatized, (D) PBS-rinsed, (E) streptavidin-flushed, (F) biotinylated protein A-flushed, (G) human IgG-flushed APSM.

The functionalized APSM chip was placed in the flow cell. The surface of APSM was rinsed thoroughly with PBS buffer solution to ensure covalent attachment to the surface and to check stability of the reflectivity measurement. 20  $\mu$ M streptavidin was injected into the flow cell, then biotinylated protein A and human IgG were flushed with PBS buffer, respectively. A constant buffer flow of 0.8 mL/min was maintained. Figure 1.10 showed the change of reflection resonance at spot 1 according to the addition of corresponding molecules. Introduction of protein fragments produced a red-shift of reflection wavelength due to an increase in the total refractive index of the porous film. The changes of

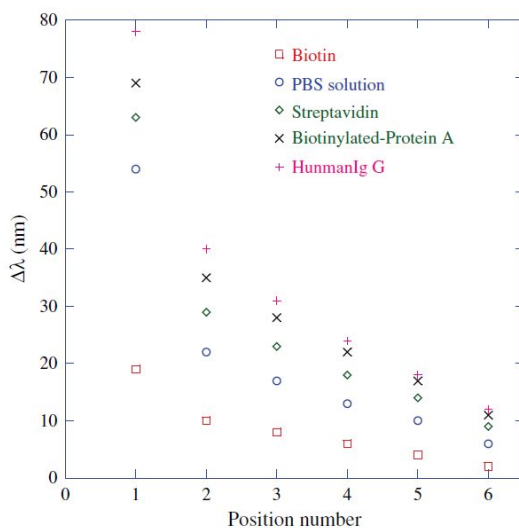


Figure 1.11 Changes of reflection wavelengths according to the step-by-step

addition of proteins in APSM.

reflection wavelengths obtained from every step and spot in APSM were monitored by reflectivity spectroscopy and summarized in Figure 1.11 The change of reflection wavelength became smaller as the lateral distance increased.

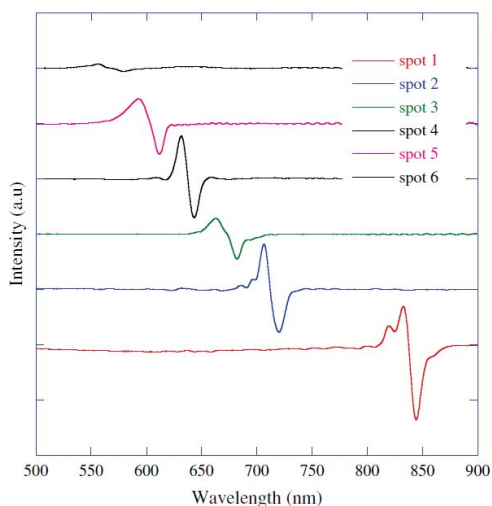


Figure 1.12 Differential plots for showing the specificity for the detection of human Ig G. at each spot in APSM.

To specify the analyte, a differnital signal obtained from the differnce between the reflction spectra before and after addition of human Ig G for each spot was shown in Figure 1.12.

## 1.4 Conclusions

The functionalized DBR PSi biosensor was prepared for the application as a label-free biosensor based on DBR PSi interferometer. Prepared DBR PSi displayed sharp reflection in the optical reflective spectra. The mean of construction of molecular architectures on DBR PSi surfaces was investigated for the step-by-step binding interaction with streptavidin, biotinylated protein A, human IgG. The subsequent introduction of streptavidin, biotinylated protein A, and human IgG resulted in the reflectivity shifted to longer wavelengths, indicative of a change in refractive indices induced by binding of biomolecules. and A 3×3 spot array of APSM modified with protein A was successfully fabricated. The reflection wavelength gradually shifted to shorter wavelength as the lateral distance increased. The changes of reflection wavelengths obtained from each step and each spot at APSM were monitored. Introduction of human Ig G produced a red-shift of reflection wavelength.

## 1.5 References

- [1]. A. G. Cullis, L. T. Canham, and P. D. J. Calcott, J. Appl. Phys. 82, 909 1997.
- [2]. H. Sohn, S. Letant, M. J. Sailor, and W. C. Trogler, J. Am. Chem. Soc. 122, 5399 2000.
- [3]. V. S.-Y. Lin, K. Motesharei, K.-P.-S. Dancil, M. J. Sailor, and M. R. Ghadiri, Science 278, 840 1997.
- [4]. A. Janshoff, K.-P. S. Dancil, C. Steinem, D. P. Greiner, V. S.-Y. Lin, C. Gurtner, K. Motesharei, M. J. Sailor, and M. R. Ghadiri, J. Am. Chem. Soc. 120, 12108 1998.
- [5]. V. Lehmann, R. Stengl, H. Reisinger, R. Detemple, and W. Theiss, Appl. Phys. Lett. 78, 589, 2001.
- [6]. L. T. Canham, M. P. Stewart, J. M. Buriak, M. Anderson, E. K. Squire, P. Allcick, and P. A. Snow, Phys. Stat. Sol. 182, 521, 2000.
- [7]. Y. Y. Li, F. Cunin, J. R. Link, T. Gao, R. E. Betts, S. H. Reiver, V. C. Sangeeta, and M. J. Sailor, Science 299, 2045, 2003.
- [8]. P. C. Searson, Advances in Electrochemical Sciences and Engineering, VCH Mannheim, Germany 112, 531, 1994.
- [9]. J. Janata, M. Josowicz, and D. M. Devaney, Anal. Chem. 66, 207, 1994.

- [10]. M. Himmelhaus and H. Takei, Sens. Actuator B-Chem. 36, 24, 2000.
- [11]. M. Cazzanelli, C. Vinegoni, and L. Pavesi, J. Appl. Phys. 85, 1760, 1999.
- [12]. C. Mazzoleni and L. Paves, Appl. Phys. Lett. 67, 2083, 1995.
- [13]. A. Brecht and G. Gauglitz, Sens. Actrators B 38, 1, 1997.
- [14]. J. Piechler, A. Brandenburg, A. Brecht, E. Wagner, and G. Gauglitz, Appl. Opt. 36, 6554, 1997.
- [15]. A. P. Abel, M. G. Weller, G. L. Duveneck, M. Ehart, and H. M. Widmer, Anal. Chem. 68, 2905, 1996.
- [16]. R. Polzius, E. Diessel, F. F. Bier, and U. Bilitewski, Anal. Biochem. 248, 269, 1997.
- [17]. J. Homola, S. S. Yee, and G. Gauglitz, Sensor. Actuat. B-Chem. 54, 3 1999.
- [18]. J. Drott, K. Lindstrom, L. Rosengren, and T. J. Laurell, Micromech. Microeng. 7, 14, 1997.
- [19]. M. P. Schwartz, S. D. Alvarez, and M. J. Sailor, Anal. Chem. 79, 327, 2007.

[20]. K. L. Beattie, W. G. Beattie, L. Mengm, S. L. Turner, R. Coral-Vazquez, D. D. Sith, P. M. McIntyre, and D. D. Dao, Clin. Chem. 41, 700, 1995.

[21]. C. Pacholski, C. Yu, G. M. Miskelly, D. Godin, and M. J. Sailor, J. Am. Chem. Soc. 128, 4250, 2006.



## Chapter Two

# Fabrication of Gradient Optical Filter Containing Anisotropic Bragg Nanostructure and Multi-Encoded Rugate Porous Silicon/Polymer Composite

## 2.1 Introduction

Photonic crystals-based sensors for detecting chemical and biological compounds have been extensively studied in recent years and present many challenges such as enhancement of specificity, increase of sensitivity, and removal of interference. This is due to their unique optical property,[1] which could be useful for a variety of applications such as chemical and biological sensors[2] or drug delivery system.[3, 4] In recent years, highly sensitive optical sensing has been achieved with a variety of PS structures, including Fabry-Perot films,[5] Bragg mirrors,[6-8] microcavities,[9] and rugate filters.[10] PS employs to detect a wide range chemical and biological compounds, including volatile organic vapors,[11] explosives,[12] chemical nerve agents,[13] DNA,[14] and proteins,[15] due to their large surface area, easy surface chemistries.<sup>16</sup> Multi-encoded rugate filters were recently developed by applying a computer-generated pseudo-sinusoidal composite current-time waveform.[17,18] The refractive index varied sinusoidally in a photonic structure of rugatestructured PS. However, PS was limited about its chemical and mechanical stability for many applications because a free-standing film was very brittle. Composite thin films might be one of candidates to eliminate these issues. Here we prepared a flexible

MRPS/polymer composite film containing a nanostructure with the complex photonic properties. Detection of organic vapors was investigated to analyze adsorption and desorption characteristics. and flexible anisotropic DBR PSi/polymer composite film displaying a rainbow colored reflection for possible applications as tunable band-rejection.

## 2.2 Experiments

### 2.2.1 Preparation of MRPS and Anisotropic DBR PSi Films

Multi-encoded rugate PS samples were prepared by electrochemical etching of heavily doped  $p^{++}$ -type silicon wafers (boron-doped, polished on the  $\langle 100 \rangle$  face, resistivity of  $0.8\text{--}1.2\text{ m}\Omega\cdot\text{cm}$ , Siltronix, Inc.). The etching solution consisted of a 3:1 volume mixture of aqueous 48% hydrofluoric acid (ACS reagent, Aldrich Chemicals) and absolute ethanol (ACS reagent, Aldrich Chemicals). Etching was carried out in a Teflon cell by using a two-electrode configuration with a Pt mesh counter electrode.

A composite waveform, the sum of three computer-generated pseudo-sinusoidal current waveforms varying between  $61.50$  and  $84.60\text{ mA}\cdot\text{cm}^{-2}$  (1000 seconds periodicity, 10 repeats), was applied as an anodization current density. Each sine component varied from  $0.40$ , to  $0.38$ , to  $0.36\text{ Hz}$  for MRPS. To etch the required sinusoidal index profile into Si, the anodization current was supplied by Keithley 2420 high-precision current source controlled by a computer to allow the formation of MRPS. Galvanostatic etching was performed in a dark room. All samples were then rinsed several times with ethanol and were dried under an argon atmosphere. Free-standing MRPS films were obtained from the silicon substrate by applying a current of  $20\text{ mA}\cdot\text{cm}^{-2}$  for 5 min in a solution of 48% aqueous HF and ethanol (1:15 by volume). The silicon surface was predominant hydride-terminated after the etching procedure. This surface was sensitive to oxidation and hydrolysis upon exposure to aqueous solution. and The DBR PSi samples were prepared by electrochemical etching of heavily-doped  $p^{++}$ -type silicon wafers (boron doped, polished on the  $\langle 100 \rangle$  face, resistivity of  $0.8\text{--}1.2\text{ m}\Omega\cdot\text{cm}$ , Siltronix,

Inc.). The etching solution consisted of a 3:1 volume mixture of aqueous 48% hydrofluoric acid (ACS reagent, Aldrich Chemicals) and absolute ethanol (ACS reagent, Aldrich Chemicals). The galvanostatic etch was carried out in a Teflon cell by applying 20 cycles of a two-electrode configuration. DBR PSi with one or two reflection bands was prepared by using periodic square-wave currents between  $5 \text{ mA}\cdot\text{cm}^{-2}$  for 90 sec and  $50 \text{ mA}\cdot\text{cm}^{-2}$  for 3 sec or between  $10 \text{ mA}\cdot\text{cm}^{-2}$  for 90 sec and  $100 \text{ mA}\cdot\text{cm}^{-2}$  for 3 sec, respectively. Free-standing anisotropic DBR PSi films were obtained from the silicon substrate by an applying of electropolishing current at  $300 \text{ mA} \cdot \text{cm}^{-2}$  for 1 min in an ethanoic 37.5% aqueous HF solution, and then at  $8 \text{ mA}\cdot\text{cm}^{-2}$  for 5 min in ethanoic 3.3% aqueous HF solution.

## 2.2.2 Preparation of MRPS and Anisotropic DBR PSi

### Composite Films

Thermally oxidized MRPS and Anisotropic DBR PSi films were obtained by heat treatment in a furnace (Thermolyne F6270-26 furnace equipped with controller) using the following parameters: initial ramp rate,  $5 \text{ }^{\circ}\text{C}/\text{min}$  to  $300 \text{ }^{\circ}\text{C}$ ; hold time, 3 h; and passive cooling to ambient temperature. For the preparation of MRPS and Anisotropic DBR PSi composite, 3 g of polystyrene (Aldrich,  $M_w = 280,000$ ) were dissolved in 20 mL of toluene (Fisher Scientific). Resulting solutions were cast onto the samples were annealed in an oven at  $50 \text{ }^{\circ}\text{C}$  for 3 hr.

### 2.2.3 Preparation of Gas Samples

For analyte exposure studies, n-hexane and methanol (98.5%, Aldrich), were purchased. Stock solutions of the molecules were prepared by freeze-pump-thaw degassed three times prior to use. All solutions were handled under dry argon.

### 2.2.4 Instruments and Data Acquisitions

The anodization current was supplied by a Keithley 2420 high-precision current source which is controlled by a computer to allow the formation of MRPS and anisotropic DBR PSi films. Interferometric reflectance spectra of MRPS and anisotropic DBR PSi were recorded by using an Ocean Optics S2000 spectrometer fitted with a bifurcated fiber optic probe. Spectra were recorded with a CCD detector in the wavelength rang 400~1200 nm. The illumination of the surface as well as the detection of the reflected light was performed along an axis coincident with the surface normal. FT-IR instrument in the diffuse reflectance mode (Spectra-Tech diffuse reflectance attachment), with diffuse reflectance absorption spectra are reported in absorbance units. The morphology of MRPS and anisotropic DBR PSi composite film was observed with cold field emission scanning electron microscope (FE-SEM, S-4700, Hitachi).

## 2.3 Results and Discussion

### 2.3.1 Results for MRPS Samples

Photonic crystals containing the rugate structure showing a high reflectivity in a specific narrow spectral region was prepared by applying a computer generated pseudo-sinusoidal current waveform.[19] Effective refractive index of rugate PS depends directly on porosity. The rugate PS prepared with a sine etching current profile possess a sinusoidally varying porosity gradient in the direction perpendicular to the plane of the filter.[18] To encode multiple rugate structures, three sine waves are summed together to create the composite waveform, which is used as an electrochemical etching current profile.[19] Therefore, multiple rugate PS might have a complex wave-formed porosity gradient rather than a simple porosity of cylindrical macro-pores in the direction perpendicular to the plane of the filter due to the sum of sine components. This complex wave-formed porosity used in the present work should give a distinct pore adsorption and desorption characteristics for sensing applications.

The composite waveform used in the present work was previously reported.<sup>20</sup> The values of amplitude and applied current density for every sine components were 23.10 and 73.05 mA, respectively. The frequency values for each of the sine components varied from 0.36 to 0.40 Hz, with a spacing of 0.02 Hz between each sine component. MRPS exhibited three sharp reflection resonances at 567, 618, and 682 nm, respectively.

MRPS film was removed by applying an electropolishing current to obtain free-standing films. The thermal oxidation of freestanding MRPS films at 300 °C converted the hydride-terminated surface into hydroxyl terminated MRPS

films. To generate a flexible MRPS film, a small drop of polystyrene solution was casted on top of the freestanding MRPS film. Schematic diagram for the fabrication of MRPS film was shown in Figure 2.1 Surface and cross-sectional SEM images of MRPS composite film were shown in Figure 2.2 The polymer-coated surface image (Fig. 2.2(a)) and a photograph (inset) of MRPS composite film illustrated that composite film was

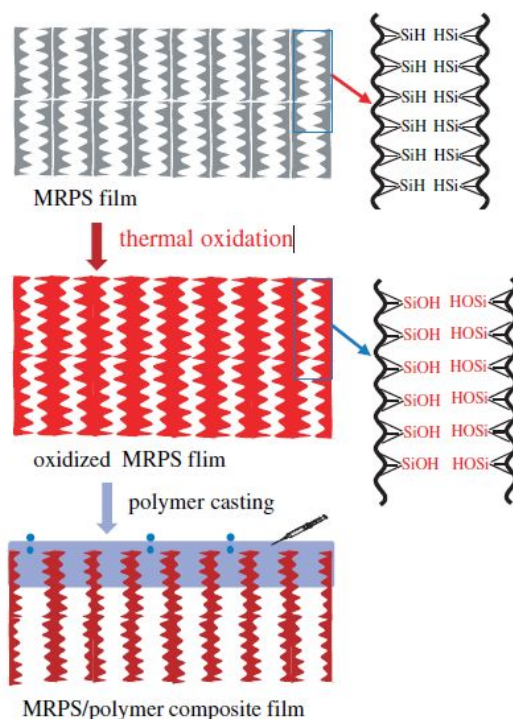


Figure 2.1 Schematic diagram for the fabrication of MRPS film.

flexible. Cross-sectional SEM image in Figure 2.2(b) showed a critical discrimination in morphology between composite layer and porous layer. The multiple rugate PS displayed a complex pore structure rather than a simple cylindrical pore structure. The porous surface image of MRPS composite film

in Figure 2.2(c) indicated that average pore size was about 100 nm. The refractive index of multiple rugate PS depends directly on porosity. The multiple rugate PS with a complex wave-formed porosity in the direction perpendicular to the plane of the filter was used for a distinct pore adsorption and desorption characteristics of analyte.

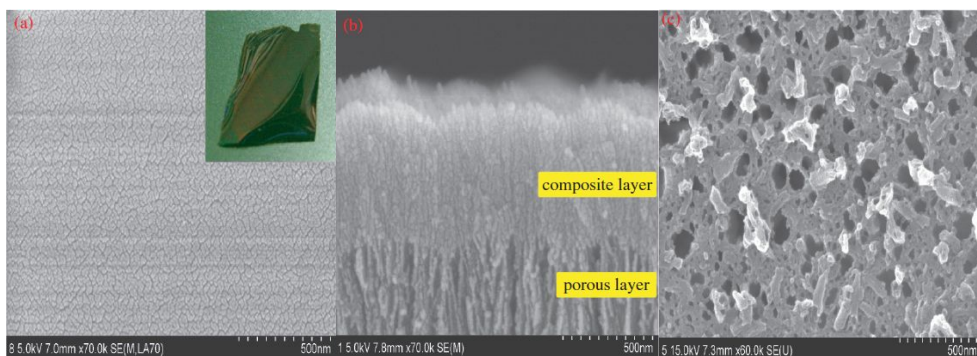


Figure 2.2 Surface and cross-sectional SEM images of MRPS/polymer composite film.

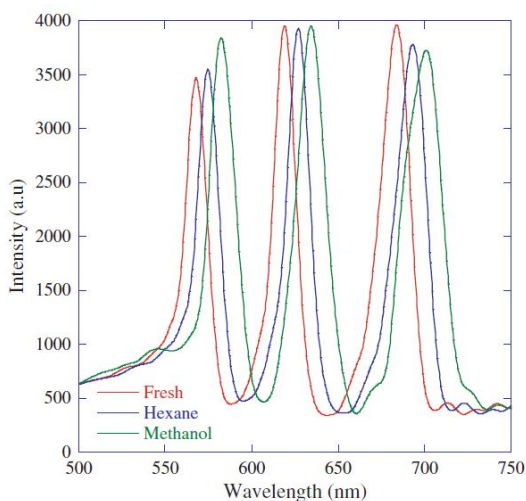


Figure 2.3 Reflection resonance spectra under exposure to different analytes



such as hexane and methanol.

Figure 2.3 showed the shift of reflection peaks under the exposure of methanol (97.48 mmHg) and n-hexane (121.26 mmHg) vapors. Three reflection peaks at 570, 620, and 685 nm shifted to the red by 7, 9, and 11 nm with hexane vapor and 15, 15, and 18 nm with methanol vapor, respectively.

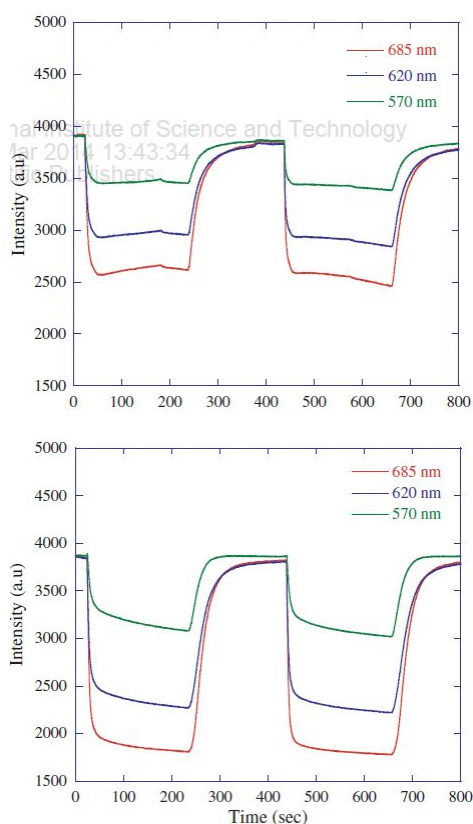


Figure 2.4 Real time responses of intensities at the fixed wavelength of reflection maxima under exposure to hexane (top) and methanol (bottom) vapors.

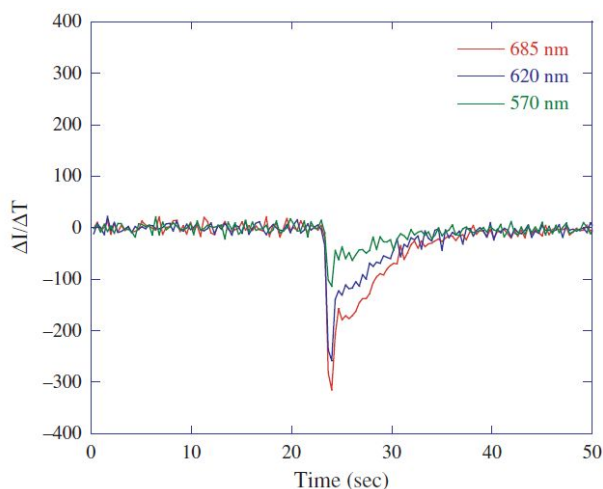


Figure 2.5 First derivatives for the capillary condensation of hexane vapor.

The reflection peaks under the exposure of methanol vapor shift to the longer wavelengths, even though the vapor pressure of methanol is less. Oxidized PS layer modified with hydroxyl functionality was a porous hydrophilic material and had a much greater affinity for hydrophilic versus hydrophobic media, since the adsorption depended on the surface property of PS layer. This result indicated that the specificity of adsorption or capillary condensation at the PS surfaces depended dramatically on the surface chemistry.

To investigate an adsorption and desorption characteristics, the change of reflection intensities at fixed wavelengths obtained from reflection minima under exposure to analytes were measured and shown in Figure 2.4.

Adsorption and desorption process exhibited a decrease and increase of reflection intensities, respectively. The repetitive exposure exhibited a consistent result to show the degree of reproducibility.

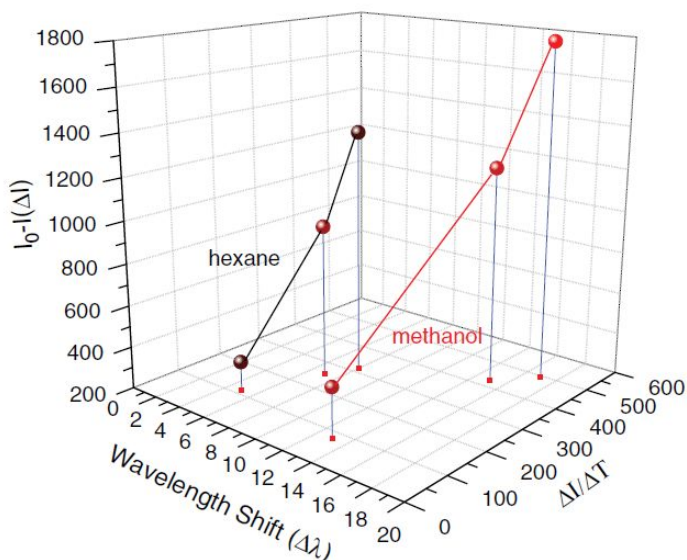


Figure 2.6 3D plot showing the relationship between the wavelength shift of the reflection bands ( $\Delta \lambda$ ,  $\Delta I/\Delta T$ , and intensity change for methanol and hexane vapors.

Figure 2.6 showed the three-dimensional relationship between the wavelength shift of the reflection bands of MRPS layer ( $\Delta \lambda$ ) and the first derivatives ( $\Delta I/\Delta T$ ) as a function of intensity change for methanol and hexane vapors. The spots were well-separated in the 3D plot.

### 2.3.2 Results for Anisotropic DBR PSi Samples

Since the discovery of DBR PSi from silicon wafer, research has been associated with emerging technologies, such as photonic crystals for optical band pass filters. DBR PSi is an attractive candidate for building nanostructured composite materials because the porosity and average pore size

can be tuned by adjusting the electrochemical preparation conditions that allow the construction of photonic crystals. DBR PSi exhibits a high reflectivity band with a Bragg wavelength,  $\lambda_{\text{Bragg}}$ , depending on the thickness of the layers ( $d_1$ ,  $d_2$ ) and the corresponding refractive indices ( $n_1$ ,  $n_2$ ). The  $m$ th order of the Bragg peak is given by

$$m \lambda_{\text{Bragg}} = 2(d_1 n_1 + d_2 n_2)$$

DBR PSi is typically prepared by an applying a computer generated periodic square-wave current between low and high current densities to the etch cell which results two distinct indices and exhibits a photonic structure of Bragg filter. In this work, anisotropic DBR PSi displaying a rainbow-colored reflection was generated by an electrochemical etching of silicon wafer with an asymmetric etching configuration as shown in Figure 2.7

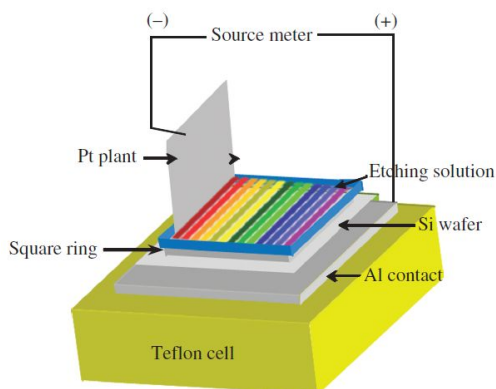


Figure. 2.7 Schematic diagram of the etch cell with plate Pt electrode for the formation of anisotropic DBR PSi.

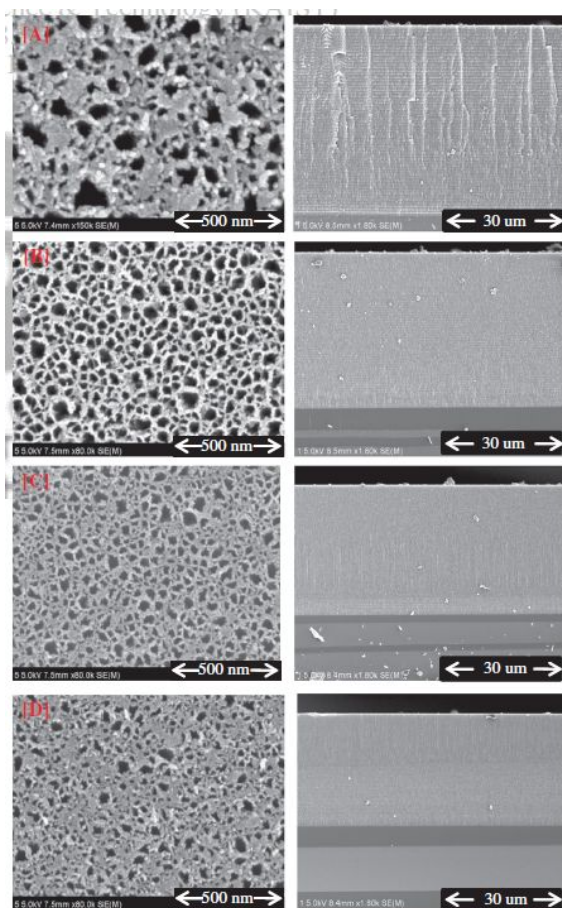


Figure. 2.8 Surface (left) and cross-section (right) images of anisotropic DBR PSi measured at the lateral distance from a point closest to the Pt counter electrode to the silicon surface: [A] at 0 mm, [B] at 30 mm, [C] at 45 mm, and [D] at 60 mm.

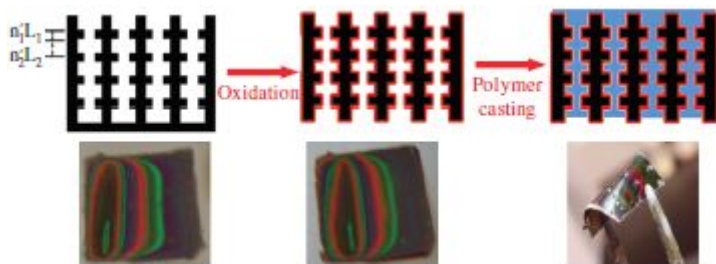


Figure. 2.9 Schematic diagram for the generation of anisotropic DBR PSi composite film and photographs of free-standing anisotropic DBR PSi film (left), oxidized anisotropic DBR PSi film (middle), and anisotropic DBR PSi composite film (right).

Surface and cross-sectional images of anisotropic DBR PSi shown in Figure 2.8 were obtained by using a cold field emission scanning electron microscope. The surface SEM images of anisotropic DBR PSi indicated that the average pore size decreased as the lateral distance (x) from the Pt counter electrode increased. The cross-sectional SEM images of anisotropic DBR PSi indicated that the anisotropic DBR PSi had a depth of several decade microns. A repeating etching process resulted in two distinct refractive indices. The thickness of anisotropic DBR PSi layer also decreased as the lateral distance increased. After the generation of anisotropic DBR PSi, freestanding anisotropic DBR PSi film was lifted off from the silicon substrate by an applying of electropolishing current and thermally oxidized in the furnace. For the anisotropic BDR composite films, polystyrene solution dissolved in toluene were cast onto the anisotropic DBR PSi films and annealed in an oven. Schematic diagram and photographs for the generation of anisotropic DBR PSi composite film were shown in Figure 2.9.

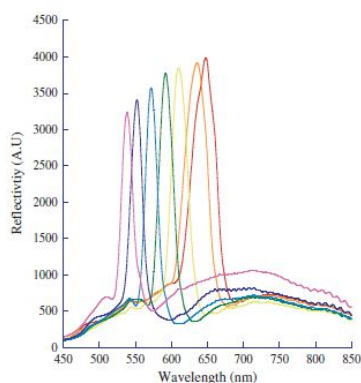


Figure. 2.10 Reflection spectra of anisotropic DBR PSi composite film as a function of lateral distance displayed reflection maxima of 650, 632, 612, 590, 574, 551, 534 nm at lateral of 0, 15, 30, 45, 60, 75, 90 mm, respectively.

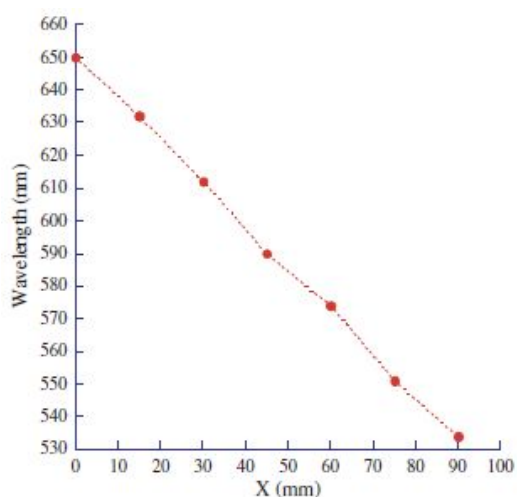


Figure. 2.11 Reflection wavelength maximum as a function of distance on the anisotropic DBR PSi composite film.

The reflection spectra of anisotropic DBR PSi composite film were shown in Figure 2.10. The reflection resonances were measured as a function of lateral distance from a point closest to the plate Pt counter electrode to a position on the silicon surface. A tungsten light source was focused onto the surface of anisotropic DBR PSi composite film with a spot size of approximately 1-2 mm. Increase of lateral distance caused the decrease of porous silicon depth and the reflection resonance to shift to shorter wavelength. Anisotropic DBR PSi with gradient porosity displayed that the reflection wavelength was spatially varied due to the uneven distribution of current across the wafer during the etching. The plot for the relationship between the reflection

wavelength maximum and the distance from the Pt electrode shown in Figure 2.11 exhibited a linear profile.

## 2.4 Conclusions

Flexible anisotropic DBR PSi composite film showing a rainbow-colored reflection was successfully fabricated by using an asymmetric etching configuration. The surface and cross-sectional images image of anisotropic DBR PSi indicated that the average pore size and the thickness of porous layer decreased as the lateral distance increased. As lateral distance increased, the reflection resonance shifted to shorter wavelength with linear relationship. and MRPS composite films having pore nanostructure were successfully fabricated by casting of polystyrene solution on the free-standing MRPS film. Surface and crosssectional SEM images of MRPS composite film were obtained to investigate the morphology composite film. The condensation and evaporation behaviors organic vapors in the nanopores of MRPS composite film were monitored by optical reflection spectroscopy in real time. The reflection bands shifted to the red upon analyte adsorption. Adsorption and desorption characteristics were investigated the change of reflection intensities at fixed wavelengths, indicating that the repetitive exposure exhibited a consistent and showed the degree of reproducibility. Behavior of capillary condensations of hexane and methanol were nearest identical. 3D relationship between the wavelength shift of the reflection bands of MRPS layer (  $\Delta \lambda$  and the first derivatives (  $\Delta I / \Delta T$  ) as a function of intensity change for methanol and hexane displayed wellseparated region in the 3D plot.



## 2.5 References

- [1]. B. H. King, T. Wong, and M. J. Sailor, *Langmuir* 27, 8576, 2011.
- [2]. H. Sohn, S. Letant, M. J. Sailor, and W. C. Trogler, *J. Am. Chem. Soc.* 122, 5399, 2000.
- [3]. Y. Y. Li, F. Cunin, J. R. Link, T. Gao, R. E. Betts, S. H. Reiver, V. Chin, S. N. Bhatia, and M. J. Sailor, *Science* 299, 2045, 2003.
- [4]. E. J. Anglin, L. Cheng, W. R. Freeman, and M. J. Sailor, *Adv. Drug Deliver. Rev.* 60, 1266, 2008.
- [5]. C. Pacholski, C. Yu, G. M. Miskelly, D. Godin, and M. J. Sailor, *J. Am. Chem. Soc.* 128, 4250, 2006.
- [6]. P. A. Snow, E. K. Squire, P. S. J. Russell, and L. T. Canham, *J. Appl. Phys.* 86, 1781, 1999.
- [7]. Y. Koh, S. Jang, J. Kim, S. Kim, Y. C. Ko, S. Cho, and H. Sohn, *Colloids Surf. A Physicochem. Eng. Aspects* 313–314, 328, 2008.
- [8]. S.-G. Kim, S. Kim, Y. C. Ko, S. Cho, and H. Sohn, *Colloids Surf. A Physicochem. Eng. Aspects* 313–314, 398, 2008.
- [9]. L. D. Stefano, L. Moretti, I. Rendina, and A. M. Rossi, *Phys. Status Solidi A-Appl. Mater.* 201, 1011, 2004.

- [10]. Y. Koh, J. Park, J. Kim, S. Jang, H.-G. Woo, and H. Sohn, J. Nanosci. Nanotechnol. 10, 3590, 2010.
- [11]. S. G Lee, Y. Koh, S. Jang, J. Kim, H.-G. Woo, S. Kim, and H. Sohn, J. Nanosci. Nanotechnol. 10, 3266, 2010.
- [12]. S. Um, M. Hwang, H. Cho, H.-G. Woo, and H. Sohn, J. Nanosci. Nanotechnol. 12, 4199, 2012.
- [13]. S. Jang, Y. Koh, J. Kim, J. Park, C. Park, S. J. Kim, S. Cho, Y. C. Ko, and H. Sohn, Mater. Lett. 62, 552, 2008.
- [14]. V. S.-Y. Lin, K. Motesharei, K. S. Dancil, M. J. Sailor, and M. R. Ghadiri, Science 278, 840, 1997.
- [15]. S. Um, B. Cho, H.-G. Woo, and H. Sohn, J. Nanosci. Nanotechnol. 11, 7061, 2011.
- [16]. J. M. Buriak, Chem. Rev. 102, 1272, 2002.
- [17]. J. Park, S. Cho, Y. C. Ko, and H. Sohn, J. Korean Phys. Soc. 50, 695, 2007.
- [18]. S. Jang, J. Kim, Y. Koh, Y. C. Ko, H.-G. Woo, and H. Sohn, J. Nanosci. Nanotechnol. 7, 4049, 2007.
- [19]. S. Um, J. Yang, T.-E. Choi, H. Cho, S. Jin, and H. Sohn, Microelectron. Eng. 89, 100, 2012.

[20]. J. Kim, Y. Koh, S. Jang, Y. C. Ko, H.-G. Woo, and H. Sohn, J. Nanosci. Nanotechnol. 7, 4165, 2007.

# Chapter Three

## Detection of Organic Vapors Based on Photoluminescent Bragg-Reflective Porous Silicon Interferometer

### 3.1 Introduction

Since the discovery of the photoluminescent porous silicon (PS),[1] it has attracted for a variety of applications such as chemical and biological sensors and drug delivery systems.[2-5] The main sensing techniques to achieve a signal transduction were capacitance,[6] resistance,[7] photo-luminescence (PL),[8] and reflectivity.[9] Typically, PS exhibiting a well-defined reflection peak in the optical reflectivity spectrum can be prepared with p-type silicon wafer under the dark condition. Detection of molecules such as toxic gases,[10-12] organic solvents,[13] DNA,[3] and proteins[14,15] can lead to a shift of reflection peak due to a change in the refractive index of PS. Luminescent PS samples are usually prepared by a galvanostatic photoetch of n-type silicon wafer under the illumination condition. The red-light emission in PS is related to quantum confinement in silicon nanocrystallites. The photoluminescence efficiency of PS is depending on the etching condition and the surface properties.[16] Organic vapors have been detected quantitatively by the quenching of PL of the quantum-confined silicon crystallites in PS.[17,18] Here, we report the preparation method of photoluminescent Bragg-reflective porous silicon (PBR PS) exhibiting both strong PL and well-defined Bragg reflection based on n-type PS. Both PL and reflectivity were used for the detection of various organic vapors.

## 3.2 Experiments

### 3.2.1 Preparation of PBR PS

PBR PS samples were prepared by an electrochemical etching of the phosphors-doped n-type Si <100> substrate (Siltronix, Inc.) with a resist in the range of 0.001~0.003  $\Omega\cdot\text{cm}$ . The etching solution consists of a 1:3 by volume mixture of absolute ethanol (ACS reagent, Aldrich Chemicals) and aqueous 48% HF (Aldrich Chemicals). The etching was carried out in a Teflon cell by using a two-electrode configuration with a Pt wire counter. PS was prepared by using a 300  $\text{mA}/\text{cm}^2$  for 1.2 seconds and 80  $\text{mA}/\text{cm}^2$  for 7.4 seconds with 50 repeats. The anodization current was supplied by a Keithley 2420 highprecision constant current source. Galvanostatic etching was performed under the illumination of 300 W tungsten filament bulb for the duration of the etching. All samples were then rinsed several times with ethanol and dried under argon atmosphere prior to use. The samples were then mounted in a glass chamber connected to a Schlenk line. The Schlenk line was connected to a direct-drive vacuum pump. The chamber was pumped to <1 mTorr between the gas exposures.

### 3.2.2 Instruments and Data Acquisitions

Steady-state PL spectra were obtained with an Ocean Optics S2000 spectrometer fitted with a fiber optic probe. The excitation source, UV LED ( $\lambda_{\text{max}} = 460 \text{ nm}$ ) was focused on the sample (at a  $45^\circ$  angle to the normal of the surface) by means of a separate fiber. The reflected light was collected at a  $90^\circ$  angle to the incident light source with a fiber optic. Spectra were recorded with a CCDdetector in the wavelength range of 400 to 900 nm. The values of percent quenching are reported as  $(I_0 - I)/I_0$ , where  $I_0$  is

the initial intensity of the luminescence in the absence of quencher of PBR PS.  $I$  is the integrated luminescence intensity of PBR PS in the presence of analyte. The luminescence intensity is integrated between 400 and 900 nm. Interferometric reflectance spectra of PBR PS samples were measured by using an Ocean Optics S2000 spectrometer. A tungsten light source was focused onto the center of the PBR PS surface. Spectra were recorded with a CCD detector in the wavelength rang 400~1200 nm. The illumination of the surface and the detection of the reflected light were performed along an axis coincident with the surface normal. At least three times of measuring were performed for each analyte studied. FT-IR spectra in the diffuse reflectance mode (Spectra-Tech diffuse reflectance attachment), are reported in absorbance units. The morphology of PBR PS was observed with a cold field emission scanning electron microscope (FE-SEM, S-4700, Hitachi).

### 3.3 Results and Discussion

PBR PS exhibiting both Bragg reflection and PL was successfully fabricated by applying a square current waveform under illumination of 300 W tungsten lamp during the etch process. The photographs of PBR PS were shown in Figure 3.1 Bragg reflector has an alternating layers of two different refractive indices and exhibits a high reflectivity band with a Bragg wavelength,  $\lambda_{\text{Bragg}}$ , depending on the thickness of the layers ( $L_1, L_2$ ) and the corresponding refractive indices ( $n_1, n_2$ ). The reflectivity is determined by the number of layer pairs and the refractive

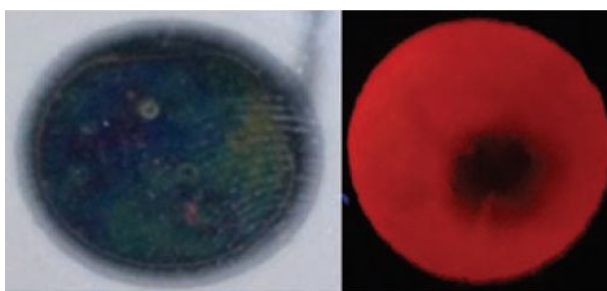


Figure. 3.1 Photographs of PBR PS under white light (left) and black light (right). Dark area at the red luminescent region is due to the quenching of the PL after exposure to water vapor.

index contrast ( $\Delta n$ ) between the layers. The Bragg reflector is characterized by its central wavelength  $\lambda_0$  (at normal incidence) and by the reflection bandwidth  $\Delta\lambda$  which is determined mainly by the index contrast. The surface and cross-sectional morphologies of PBR PS shown in Figure 3.2 were obtained using FE-SEM. FESEM surface image of PBR PS displayed very stable and even surface with the pore sizes in the range of 10 to 20 nm. The cross-sectional image of PBR PS illustrated that the 50 period PBR PS had a depth of 20.5  $\mu\text{m}$ . The repeating etch process resulted in two different

refractive indices. Optical reflectance and PL shown in Figure 3.3 were measured to investigate the optical properties of PBR PS. The PBR PS displayed a strong reflection resonance at 761 nm with full width at half maximum (FWHM) of 16 nm in reflective interference spectrum and a strong broad red PL at 640 nm in PL spectrum.

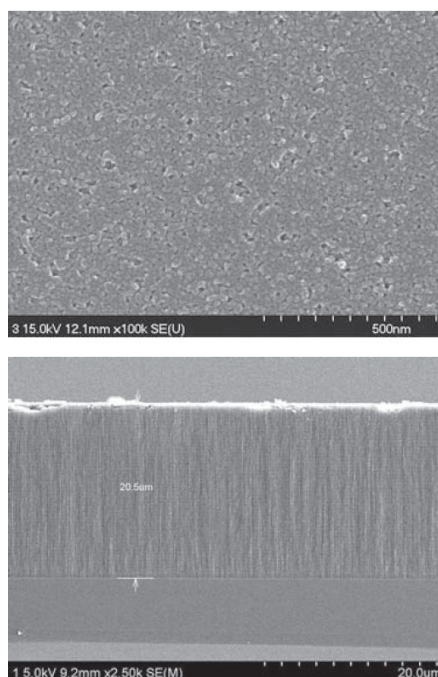


Figure. 3.2 Surface (top) and cross-section (bottom) SEM images of PBR PS.

FT-IR spectroscopy was used to characterize the surface of PBR PS. FT-IR spectrum of PBR PS shown in Figure 3.4 displayed vibrational frequencies associated with the surface Si.H species at  $\nu(\text{Si-H}) = 2085$ ,  $\nu(\text{Si-H}_2) = 2117$ ,  $\nu(\text{Si-H}_3) = 2145$ ,  $\delta(\text{Si-H}) = 908$ ,  $\delta(\text{Si-Si}) = 611 \text{ cm}^{-1}$ , respectively.

The PBR PS samples were placed in an exposure chamber fitted with an optical window. Since the surface of PBR PS was H-terminated, three different organic substances having different vapor pressures and groups such



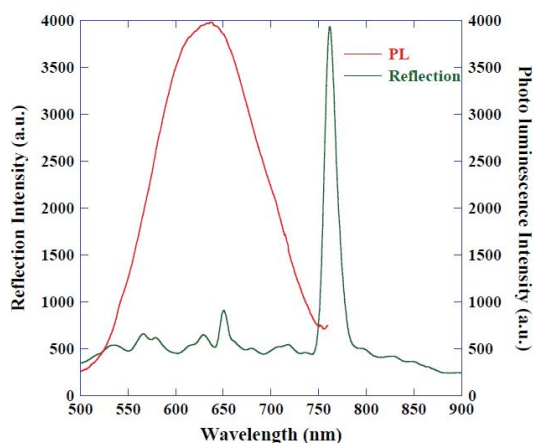


Figure. 3.3 Reflectivity (green line) and PL (red line) spectra of PBR PS.

as aromatics, alcohol, and ketone were used for evaluating their adsorption behaviors. The PBR PS samples were exposed to a vapor flux of acetone (184 mmHg at 25 °C), methanol (97 mmHg at 25 °C), and benzene (80 mmHg at 25 °C), respectively. Optical reflectivity spectra were measured using a tungsten.halogen lamp and CCD spectrometer fitted with a fiber optic. As shown in Figure 3.5, the capillary condensation of the organic vapors in the pores of PBR PS lead an increase in the refractive indices of the porous medium which resulted in the shift of reflectivity to the longer wavelengths. The shift range of reflectivity of PBR PS was depended on the vapor pressure of organic molecules regardless of their functionalities. Such a red shift is the characteristic of an increase in the average refractive index of the multilayers, consistent with the replacement of a significant amount of empty pore volume with organic vapors.

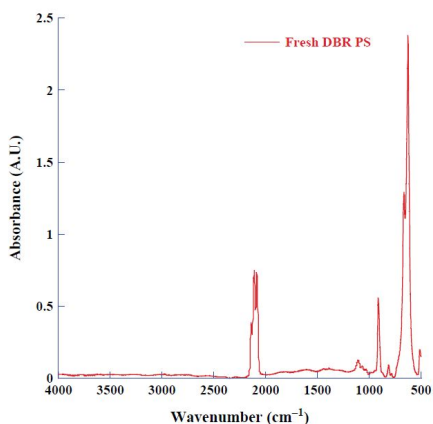


Figure. 3.4 FT-IR spectrum of PBR PS.

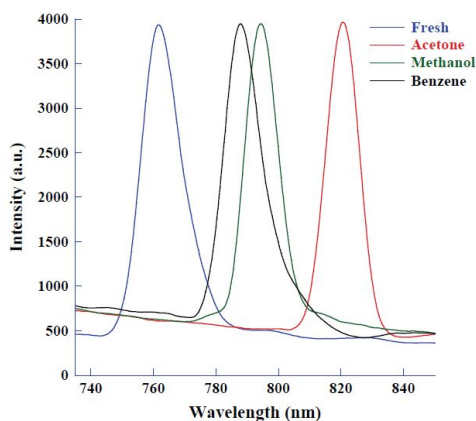


Figure. 3.5 Reflection spectra of fresh PBR PS(blue,  $\lambda = 761$  nm) and PBR PS under a flux of benzene (black,  $\lambda = 788$  nm,  $\Delta\lambda = 27$  nm), methanol (green,  $\lambda = 796$  nm,  $\Delta\lambda = 35$  nm), and acetone (red,  $\lambda = 809$  nm,  $\Delta\lambda = 48$  nm).

The strong broad red PL of PBR PS is due to the quantum confinement of silicon nanocrystallites in PS. To investigate the quenching efficiency of PL, the steady-state PL spectra were measured under the exposure of three different organic vapors as shown in Figure 6. The quenching of PL is

resulted from the luminescent chromophore in PBR PS to a weakly chemisorbed organic molecule. According to Figure 3.6, the organic samples with higher vapor pressure exhibited the greater quenching of PL, however it was not clear if the functionalities of organic molecules had affected the quenching phenomenon. When the gaseous organics were withdrawn, the PL was completely recovered to the initial state.

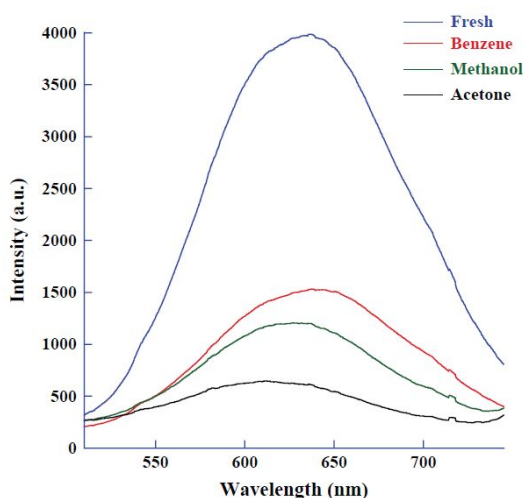


Figure. 3.6 PL spectra of PBR PS under a flux of acetone (black), methanol (green), and benzene (red).

To further discriminate the relationship between the vapor pressure and the functionalities, the PBR PS was exposed to the three different analytes at different vapor pressures.

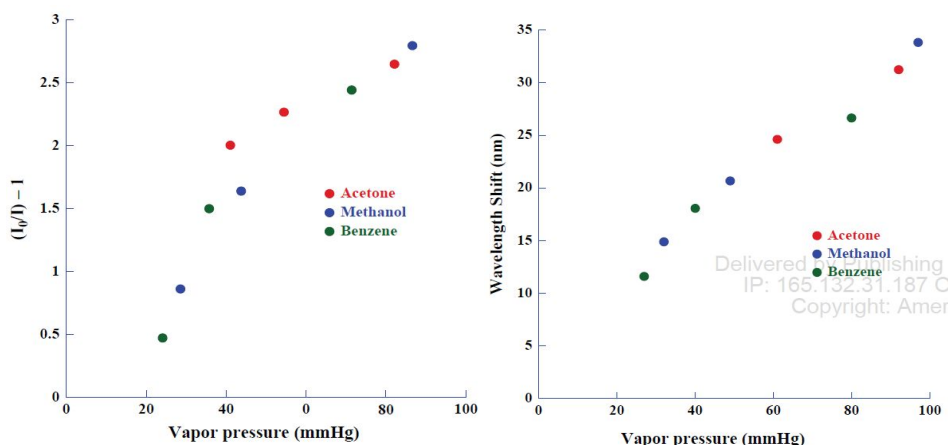


Figure. 3.7 A plot for the relationship between the different vapor pressures of three analytes and the change of Bragg reflection wavelength (left). Stern-Volmer plots for three different analytes at various vapor pressures (right).

A plot for the relationship of Bragg reflection wavelength with different vapor pressures of three analytes, was shown in Figure 3.7 (left). Generally, the shift of Bragg reflection wavelength depends on refractive index, functionalities, and vapor pressure of the analyte as well as the surface characteristics and the pore diameter of PS. Since the latter parameters of PBR PS were fixed, the shift of reflection wavelength is related to parameters of analytes. A linear relationship was observed for all analytes. Analyte with a higher vapor pressure exhibited a greater change of Bragg reflection wavelength in reflectance spectra. This result indicated that the shift of Bragg reflection wavelength depended only on the vapor pressure of analytes, not their functionalities of molecules. Stern-Volmer plots for three different analytes at various vapor pressures are shown in Figure 3.7 (right). Typically, a dynamic Stern-Volmer quenching model yields straight lines between the quenching of PL and quencher concentration.

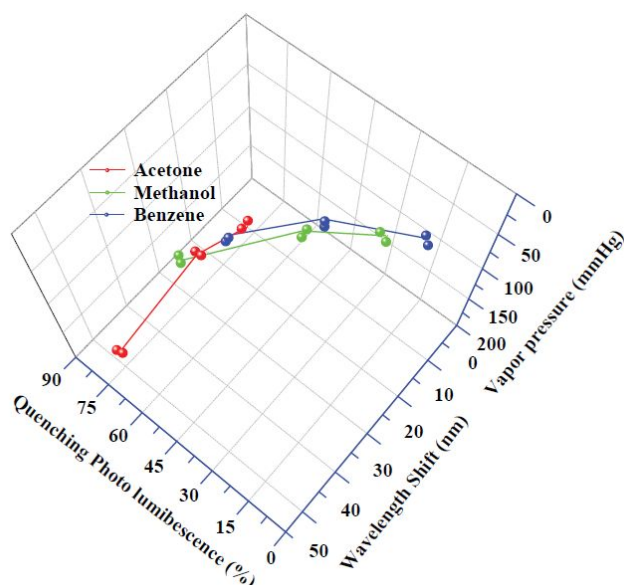


Figure. 3.8 3D plot showing the relationship between the wavelength shift of the reflection peak and quenching PL as a function of different vapor pressures of three analytes such as acetone (red), methanol (green), and benzene (blue).

A linear relationship was observed for the individual analyte, however Stern-Volmer constants for the three analytes were not identical to each other. This result indicated that the quenching of PL depended on not only the vapor pressure of analytes, but also the functionalities of organic molecules. Since the quenching of PL is caused by an adsorption of organic vapors onto the surface of silicon nanocrystallites in the pores of PBR PS, the functionalities of analytes were related to the quenching degree of PL. Therefore, the quenching degree of PL can be one of the important factors to determine a specific analyte. Figure 3.8 showed the three-dimensional plot to specify the analyte using the relationship between the shifts of reflection wavelength, the quenching of PL, and the vapor pressure of three different analytes. The PBR PS was exposed to each analyte three times. Each line connected by a cluster of points was well separated from each other in the

space, which represented the characteristics of the three analytes measured. The smaller the area of the clusters indicates the better the reproducibility. Again these measurements are potential indicators to differentiate analytes for sensing.

### 3.4 Conclusions

The preparation of PBR PS exhibiting both strong PL and Bragg reflection was reported. Both PL and reflectivity were used for the detection of different organic molecules having different functionalities such as acetone, methanol, and benzene. The relationship between the vapor pressure of analyte, Bragg reflection, and quenching of PL demonstrated the potentiality of PBR PS sensors for the detection of different organic vapors.

### 3.5 References

- [1]. L. T. Canham, Appl. Phys. Lett. 57, 1046, 1990.
- [2]. H. Sohn, S. Letant, M. J. Sailor, and W. C. Trogler, J. Am. Chem. Soc. 122, 5399, 2000.
- [3]. V. S. Lin, K. Motesharei, K. S. Dancil, M. J. Sailor, and M. R. Ghadiri, Science 278, 840, 1997.
- [4]. Y. Koh, S. Jang, J. Kim, S. Kim, Y. C. Ko, S. Cho, and H. Sohn, Colloid. Surface A 313.314, 328, 2008.
- [5]. C. Park, J. Kim, S. Jang, H.-G. Woo, Y. C. Ko, and H. Sohn, J. Nanosci. Nanotechnol. 10, 3375, 2010.
- [6]. R. C. Anderson, R. S. Muller, and C. W. Tobias, Sensor Actuat. A-Phys. A21-23, 835, 1990.
- [7]. M. Ben-Chorin, A. Kux, and I. Schechter, Appl. Phys. Lett. 64, 481, 1994.
- [8]. J. M. Lauerhaas and M. J. Sailor, Science 261, 1567, 1993.
- [9]. C. L. Curtis, V. V. Doan, G. M. Credo, and M. J. Sailor, J. Electrochem. Soc. 140, 3492, 1993.



- [10]. S. Kim, B. Cho, and H. Sohn, *Nanoscale Res. Lett.* 7, 527, 2012.
- [11]. S. Jang, J. Kim, Y. Koh, Y. C. Ko, H.-G. Woo, and H. Sohn, *J. Nanosci. Nanotechnol.* 7, 4049, 2007.
- [12]. S. Jang, Y. Koh, J. Kim, J. Park, C. Park, S. J. Kim, S. Cho, Y. C. Ko, and H. Sohn, *Mater. Lett.* 62, 552, 2008.
- [13]. S. G. Kim, S. Kim, Y. C. Ko, S. Cho, and H. Sohn, *Colloid. Surface A* 313–14, 398, 2008.
- [14]. K.-P. S. Dancil, D. P. Greiner, and M. J. Sailor, *J. Am. Chem. Soc.* 121, 7925, 1999.
- [15]. Y. Koh, J. Park, J. Kim, S. Jang, H.-G. Woo, and H. Sohn, *J. Nanosci. Nanotechnol.* 10, 3590, 2010.
- [16]. B. Cho, S. Jin, B.-Y. Lee, M. Hwang, H.-C. Kim, and H. Sohn, *Microelectron. Eng.* 89, 92, 2012.
- [17]. J. H. Song and M. J. Sailor, *J. Am. Chem. Soc.* 119, 7381, 1997.
- [18]. S. G. Lee, Y. Koh, S. Jang, J. Kim, H.-G. Woo, S. Kim, and H. Sohn, *J. Nanosci. Nanotechnol.* 10, 3266, 2010.

# **Part II.**

# **FLUORESCENT**

# **NANOSENSORS BASED**

# **ON SILICON**

# **QUANTUM DOTS**

## Chapter One

# Fabrication and Characterization of Photoluminescent Silicon Nanoparticles for Drug Delivery Applications

## 1.1 Introduction

The development of nanotechnologies in life science has been strongly affecting the biomedicine, both in diagnostics and therapy.[1,2] Since nanotechnology offers a suitable method of site-specific and time-controlled delivery of drugs, significant efforts have been devoted to use the potentials of nanotechnology in drug delivery.[3,4] In recent years, pharmaceutical nanotechnology focuses on formulating therapeutically active agents in biocompatible nanoforms. PSi has been investigated for applications in chemical and biological sensors and biomedical devices.[5,6] Since Canham reported the *in vivo* use of PSi and demonstrated its resorbability and biocompatibility,[7,8] PSi has been employed as host matrices to demonstrate *in vivo* release of the steroid dexamethasone, ibuprofen, doxorubicin, and many other drugs.[9-14] Recently, Sailor et al. reported that PSi nanoparticle can be used for cancer therapy.[15] CPT, a pentacyclic alkaloid, isolated first by Wall and co-workers from the Chinese tree *Camptotheca acuminata*, shows potent cytotoxic activity against a range of tumor cell lines.[16,17] However, administration of this drug was accompanied by severe side effects, due to its poor water solubility. CPT polymeric drugs were reported to improve the therapeutic efficacy in the controlled release of drugs.[18] In this paper, photoluminescent Si nanoparticles (NPs) derivatized with CPT were prepared and the release pattern was observed for drug delivery applications.

## 1.2 Experiments

### 1.2.1 Preparation of Photoluminescent PSi

n-Type silicon wafer (P-doped, orientation, <100>, resistivity of 1.10  $\Omega$ -cm, Siltronix, Inc.) was used to fabricate photoluminescent PSi by an anodic etch in ethanolic HF consisted of a 1:1 volume mixture of aqueous 48% hydrofluoric acid (Aldrich) and absolute ethanol (Aldrich). The galvanostatic etch was carried out in a Teflon cell by using a two-electrode configuration with a Pt counter electrode. The anodization current of 150 mA for 300 seconds was supplied by a Keithley 2420 high-precision constant current source under the illumination with a 300 W tungsten filament bulb for the duration of etch. All samples after etching were rinsed several times with ethanol and dried under argon atmosphere prior to use.

### 1.2.2 Surface Oxidation of Photoluminescent PSi

To obtain the surface-oxidized luminescent PSi, fresh PSi samples were electrochemically treated with the current of 150 mA for 60 seconds in water and sodium chloride. It is noted that the thermal oxidation of fresh luminescent PSi exhibited abrupt decrease of PL.

### 1.2.3 Preparation of CPT-Derivatized Silicon Nanoparticles

Surface-oxidized photoluminescent PSi was placed in Schlenk flask with 1.4 mg of (s)-(+)- CPT (0.005 mmol, Aldrich Chemicals) dissolved in 20 mL of

toluene under argon atmosphere. The mixture solution was stirred at 40 °C for 5 hrs. The reaction mixture was allowed to stir at room temperature. Afterward the CPT-derivatized PSi was rinsed successively with ethanol, toluene, and acetone and subsequently dried under a stream of nitrogen. The CPT-derivatized PSi was made into particles by ultrasonic fracture in toluene for 3 hrs and the mixture solution was centrifuged to obtain CPT-derivatized photoluminescent Si Nps.

## 1.2.4 Instrumentation and Data Acquisition

The anodization current was supplied by a Keithley 2420 high-precision current source meter. Steady-state PL spectra were obtained with an Ocean Optics S2000 spectrometer fitted with a fiber optic probe. The excitation source was a LED ( $\lambda_{\text{max}} = 460 \text{ nm}$ ) focused on the sample (at a 45° angle to the normal of the surface) by means of a separate fiber. Light was collected at a 90° angle to the incident light source with a fiber optic. Spectra were recorded with a CCD-detector in the wavelength range of 400-900 nm. FT-IR instrument in the diffuse reflectance mode (Spectra-Tech diffuse reflectance attachment), with diffuse reflectance absorption spectra are reported in absorbance units. Morphologies of photoluminescent PSi were observed with a cold field emission scanning electron microscope (FE-SEM, S-4800, Hitachi). UV-vis absorption and PL of CPT-derivatized Si NPs were measured by Shimadzu UV-2401 spectrophotometer and Perkin-Elmer luminescence spectrometer LS 50B, respectively. CPT released in aqueous buffer solution was measured by UV-vis spectrometer.

## 1.3 Results and Discussion

PSi consisted of a large number of interconnected Si nanocrystallites whose surface is almost entirely covered with hydrogen atoms. An anodic etch of n-type silicon wafer with resistivities of 1-10  $\Omega$  cm in ethanolic HF solution generally produced a strong visible red photoluminescent PSi possibly due to the photoetch. The red PL is due to the quantum confinement of silicon nanocrystallites

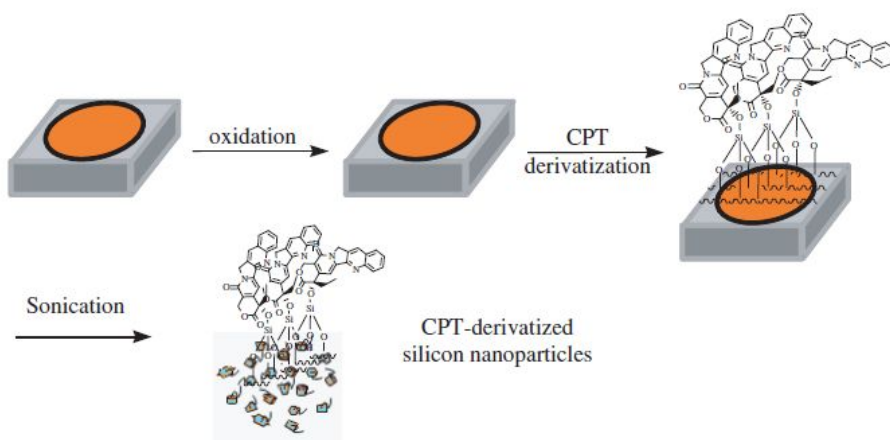


Figure. 1.1 Schematic diagram for the preparation of CPT-derivatized Si Nps.

in porous silicon. In this work, photoluminescent PSi has been successfully fabricated by using an applied current density of 150 mA/cm<sup>2</sup> for 5 min.

Schematic diagram for the preparation of CPTderivatized Si Nps is shown in Figure 1.1 To obtain a chemically bonded Si Nps with CPT, the surface of PSi was oxidized. Since the thermal oxidation of PSi at 300 °C converted the hydride-terminated surface into hydroxyl terminated silicon dioxide porous film, the thermal oxidized PSi displayed almost no red PL. Surface-oxidized red luminescent

PSi was obtained by an electrochemical treatment of fresh PSi with the current of 150 mA for 60 seconds in water and sodium chloride. Figure 1.2 showed the condensation reaction of surface-oxidized PSi with CPT to give CPT-derivatized PSi. Figure 3(a) showed that the FT-IR spectrum of freshly etched PSi displayed a characteristic broad band centered at 2100 and 900  $\text{cm}^{-1}$  for the (Si-H) stretching vibration and (Si-H) bending vibration, respectively. After the electrochemical oxidation of PSi, the presence of Si.OH was determined by FT-IR measurement as shown in Figure 3(b). The electrochemical oxidation of the porous silicon layer resulted significant loss of intensity of the (Si-H) modes in the infrared spectrum at 2150  $\text{cm}^{-1}$ , but vibrational bands due to silicon hydride, (Si-OH), and oxygen-back-bonded silicon hydride, (OSi-H) and (OSi-H) modes, grew at 3000 to 3500, 2300, and 850  $\text{cm}^{-1}$ , respectively. Surface derivatization of surfaceoxidized PSi with CPT generated a surface-bound CPT. FT-IR spectrum shown in Figure 1.3(c) displayed additional band characteristic of CPT (the aromatic C=C band of  $\nu$  (C= C) at 1630  $\text{cm}^{-1}$ .

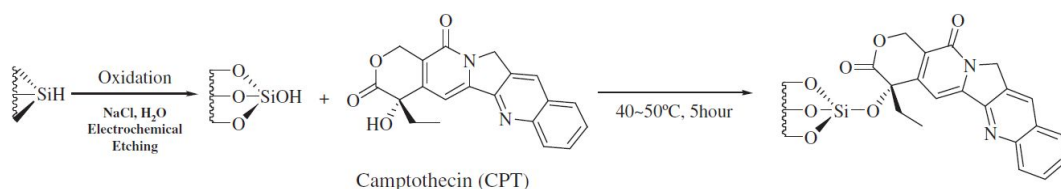


Figure. 1.2 Chemical reactions for the surface derivatization of Si NPs with CPT.

Absorption measurements to analyze CPT release pattern from the CPT-derivatized PSi in buffer solution were achieved as a function of time at fixed wavelength of 369 nm which was the absorption maxima of CPT (Fig. 1.4). CPT release was measured for 12 hr. The CPT-derivatized PSi displayed

nonlinear release profile. The release of CPT in pH = 9 was faster than in lower pH. CPT-derivatized PSi were sonicated and centrifuged in toluene solution to make Si NPs. Surface SEM images of CPT-derivatized Si NPs shown in Figure 1.5 indicated

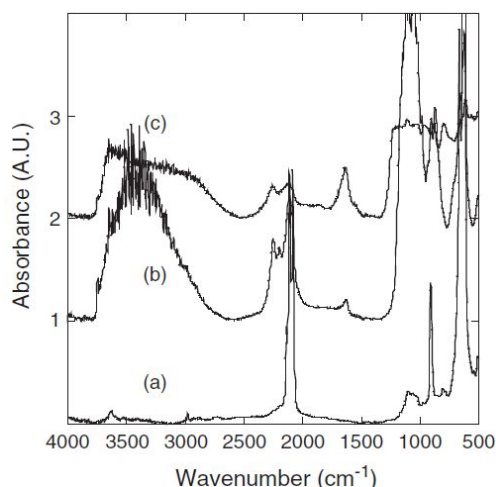


Figure. 1.3 FT-IR spectra of fresh PSi sample (a), surface-oxidized PSi sample (b), and CPT-derivatized PSi sample (c).

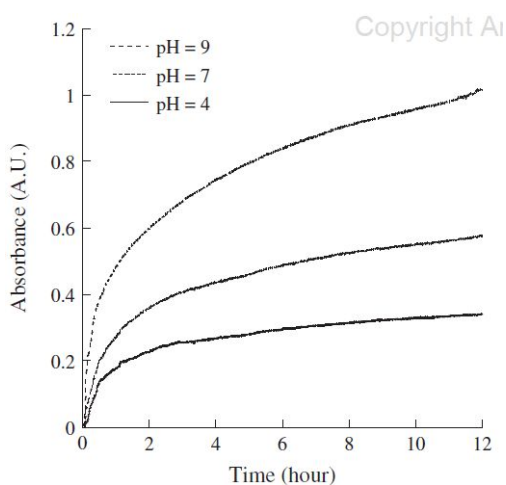




Figure. 1.4 CPT release in buffer solutions as a function of time, measured by using an absorption band at 369 nm.

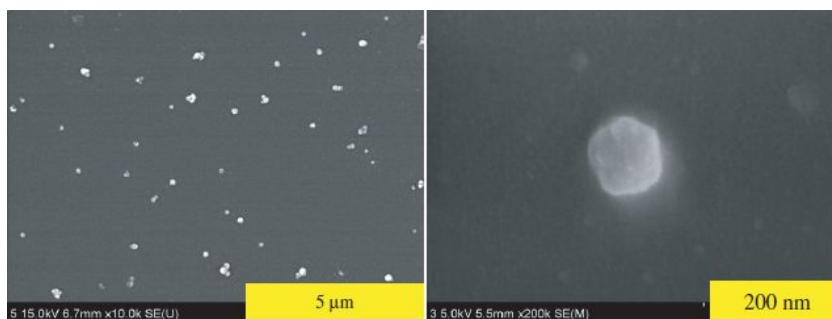


Figure. 1.5 FE-SEM images of CPT-derivatized Si NPs.

that the average size of CPT-derivatized Si NPs was about 100 nm with narrow size distribution. Absorption and PL spectra shown in Figure 1.6 were measured for CPT, Si NPs, and CPT-derivatized Si NPs. CPT and Si NP showed their fluorescences at 425 and 625 nm, respectively. When CPT was chemically bonded with Si NPs, the PL of CPT disappeared due to the energy migration from CPT to Si NPs. Stability of CPT-derivatized Si NPs were measured in PBS buffer solution and shown in Figure 1.7. PL of CPT-derivatized Si NPs remained unchanged for 12 hr, indicating that Si NPs were quite stable.

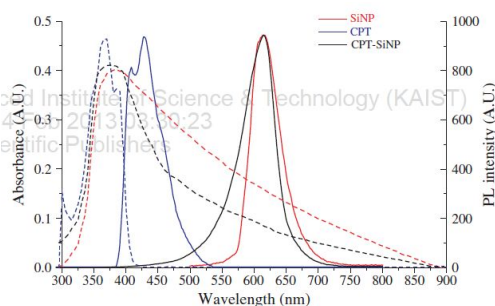


Figure. 1.6 UV-vis absorption (dashed line) and PL (solid line) spectra for CPT (red), Si NPs (blue), and CPT-derivatized Si NPs (black).

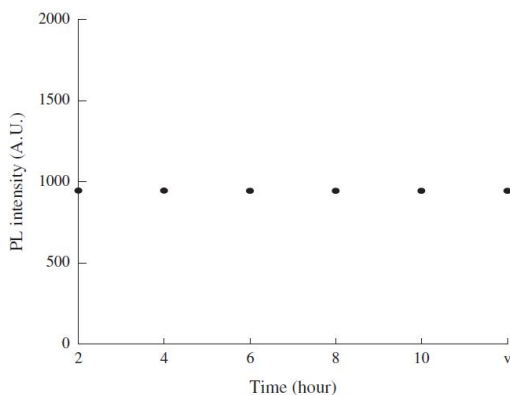


Figure. 1.7 Plot for the stability of CPT-derivatized Si NPs in PBS buffer solution.

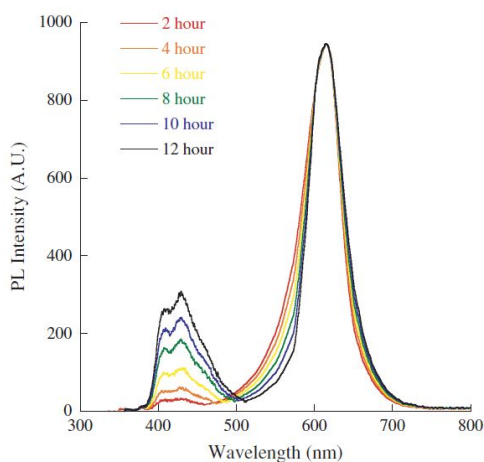


Figure. 1.8 PL spectra during the release of CPT from Si NPs.

PL measurements to analyze CPT release from the CPTderivatized Si NPs in buffer solution were investigated and shown in Figure 1.8. As the release of

CPT from Si NPs by the hydrolysis between PSD and CPT progressed, the PL of CPT increased, but that of Si NPs remained unchanged. This result indicated that Si NPs might be an excellent fluorescent probe for drug delivery materials.

## 1.4 Conclusions

CPT-derivatized Si Nps were successfully synthesized for drug delivery application and characterized by SEM and FT-IR spectroscopy. To analyze CPT release pattern, absorption measurements from the CPT-derivatized PSi were achieved as a function of time. The release of CPT was faster in higher pH value. Stability of CPT-derivatized Si NPs was measured in PBS buffer solution and PL was very stable. PL measurements of CPT-derivatized Si NPs indicated that the PL of Si NPs remained unchanged during the release process.

## 1.5 References

- [1]. D. A. LaVan, T. McGuire, and R. Langer, *Nat. Biotechnol.* 21, 1184, 2003.
- [2]. B. Ziaie, A. Baldi, M. Lei, Y. Gu, and R. A. Siegel, *Adv. Drug Deliv. Rev.* 56, 145, 2004.
- [3]. L. Vaccari, D. Canton, N. Zaffaroni, R. Villa, M. Tormen, and E. D. Fabrizio, *Microelectron. Eng.* 83, 1598, 2006.
- [4]. E. J. Anglin, L. Cheng, W. R. Freeman, and M. J. Sailor, *Adv. Drug Deliv. Rev.* 60, 1266, 2008.
- [5]. H. Sohn, S. Letant, M. J. Sailor, and C. Trogler, *J. Am. Chem. Soc.* 122, 5399, 2000.
- [6]. C. A. Canaria, M. Huang, Y. Cho, J. L. Heinrich, L. I. Lee, M. J. Shane, R. C. Smith, M. J. Sailor, and G. M. Miskelly, *Adv. Funct. Mater.* 12, 495, 2002.
- [7]. L. T. Canham, *Adv. Mater.* 7, 1033, 1995.
- [8]. L. T. Canham, C. L. Reeves, D. O. King, P. J. Branfield, J. G. Crabb, and M. C. L. Ward, *Adv. Mater.* 8, 850, 1996.
- [9]. E. J. Anglin, M. P. Schwartz, V. P. Ng, L. A. Perelman, and M. J. Sailor, *Langmuir* 20, 11264, 2004.

- [10]. C. Charnay, S. Begu, C. Tourne-Peteilh, L. Nicole, D. A. Lerner, and J. M. Devoisselle, *Eur. J. Pharm. Biopharm.* 57, 533, 2004.
- [11]. J. L. Coffey, J. L. Montchamp, J. B. Aimone, and R. P. Weis, *Phys. Status Solidi A-Appl. Res.* 197, 336, 2003.
- [12]. J. Salonen, A. M. Kaukonen, J. Hirvonen, and V. P. Lehto, *J. Pharm. Sci.* 97, 632, 2008.
- [13]. C. Park, J. Kim, S. Jang, H.-G. Woo, Y. C. Ko, and H. Sohn, *J. Nanosci. Nanotechnol.* 10, 3375, 2010.
- [14]. S. Jang, Y. Koh, H.-G. Woo, and H. Sohn, *J. Nanosci. Nanotechnol.* 11, 1328, 2011.
- [15]. L. Xiao, L. Gu, S. B. Howell, and M. J. Sailor, *ACS Nano* 5, 3651, 2011.
- [16]. M. E. Wall, M. C. Wani, K. H. Cook, A. T. McPhail, and G. A. Sim, *J. Am. Chem. Soc.* 88, 3888, 1966.
- [17]. M. E. Wall and M. C. Wani, *Cancer Res.* 55, 753, 1995.
- [18]. N.-J. Lee, S.-J. Lee, S.-H. Kim, Y.-S. Kang, S.-B. Moon, H. Sohn, K.-T. Kang, and E. A. Theodorakis, *Eur. Polym. J.* 40, 1291, 2004.

## Chapter Two

# Silicon quantum dot sensors for an explosive taggant, 2,3-dimethyl-2,3-dinitrobutane (DMNB)

## 2.1 Introduction

Detection of high explosives is an important subject in areas of homeland security, military applications, munition remediation sites, and environmental safety.<sup>1</sup> However plastic bonded explosives containing nitramines such as RDX and HMX are very hard to detect due to their extremely low vapor pressure. Therefore all the explosives are currently required to incorporate 0.5% to 1.0% of 2,3-dimethyl-2,3-dinitrobutane (DMNB) as a tagging agent to detect substances containing high explosives easily.[2] Although various detection methods for high explosives have been extensively investigated,[1,3-6] detection of DMNB remains a great challenge. DMNB has a relatively high vapor pressure of approximately [2-7] ppm ( $2.07 \times 10^{-3}$  Torr at 25 °C), but it possesses unfavourable reduction potential (-1.7 V vs. SCE) and weak binding to the sensory materials due to its three-dimensional molecular structure and lack of p-stacking interactions.[7] The current detection methods typically involve canines,[8] or sophisticated analytical instruments.[9] The most common methods include ion mobility spectrometry (IMS), mass spectrometry (MS), and gas chromatography (GC).[10] However, the current explosive detecting systems are rather difficult to use, because they are time consuming and require a large space as well as are expensive. This calls for a small and easy to use device that can be massively deployed

where needed. Fluorescence quenching of sensory materials based on the donor-acceptor electron-transfer mechanism might be a simple and promising alternative procedure. For the detection of DMNB, microporous metal-organic frameworks (MMOFs), [2,11] (salophen) Zn complexes, [12] and amplifying fluorescent polymers (AFPs) [7] have recently been reported.

## 2.2 Experiments

Nanosized silicon materials have been receiving ever increasing popularity because of their advantages such as non-toxicity, relatively low cost, and easy integration into well-established industrial silicon processes when compared to the well-established II.VI quantum dots (QDs), which made researchers in many different fields pay attention to their application in biomedical imaging, drug delivery carriers, and chemical and bio sensors. [13-16] For the past few decades, vigorous research studies on group II.VI QDs [17] led to the development of large-scale preparation of relatively monodisperse quantum dots, [18] quantum dot arrays, [19] light-emitting diodes, [20] and fluorescent probes. [21] Although the non-toxicity and abundance of silicon make the bottom-up synthesis of silicon QDs (Si QD) quite desirable for many biological and sensing applications, the research studies have not been as aggressive as on group II.VI QDs due to the limitation of synthetic methods. Recently, efficient solution syntheses for Si QDs were reported by the reaction of the Zintl salt with  $\text{SiCl}_4$  [22] or  $\text{NH}_4\text{Br}$  [23] as well as the solution reduction of silicon halides by alkaline metal naphthalenide, [24] and sodium/benzophenone. [25] In this study, we conducted research on sensing applications for explosive taggants by utilizing bottom-up synthesis of Si QDs [26] and discussed its mechanism.



## 2.3 Results and Discussion

Even though research on the bottom-up synthesis by magnesium silicide of blue luminescent Si QDs has been well discussed and reported, the synthesis of green luminescent Si QDs has yet not been reported. Blue and green luminescent Si QDs were successfully synthesized by the reaction of  $\text{Mg}_2\text{Si}$  with ethylenediamine dihydrochloride after 48 and 72 hours reflux, respectively. Since trioctylphosphineoxide in the CdSe QD synthesis controlled the growth and size distribution of QDs, an attempt to use ethylenediamine dihydrochloride as both the reducing agent and the surfactant was made. Here we report for the first time the use of blue and green luminescent Si QDs for the successful detection of DMNB (Fig. 2.1).[27] Photoluminescence of Si QDs, as seen in Fig.

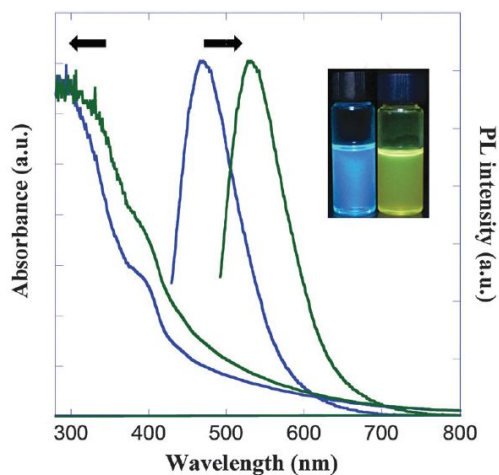


Fig 2.1 UV absorption band and PL spectra of blue ( $\lambda_{\text{max}} = 460 \text{ nm}$ ) and green ( $\lambda_{\text{max}} = 520 \text{ nm}$ ) luminescent Si QDs, showing blue and green PL

under a UV light lamp (inset).

Si QDs were characterized by HRTEM as seen in images in Fig. 2a, showing silicon nanoparticles ranging from 2 nm to 3 nm, as well as a SAED pattern indicating pseudo-hexagonal symmetry of the  $\langle 111 \rangle$  face of Si (Fig. 2.2b) and fast Fourier transform image (Fig. 2.2c). The diameters of Si QDs measured by dynamic light scattering (DLS) revealed that the average particle diameters for blue and green luminescent Si QDs were 2 and 3 nm, respectively. The FT-IR spectrum of Si QDs displayed a characteristic broad

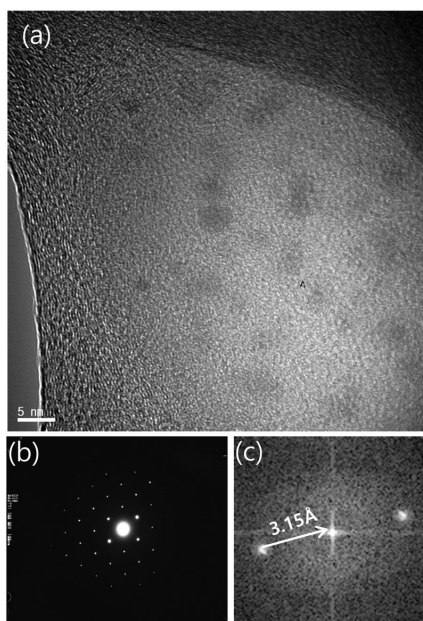


Figure. 2.2 HRTEM image (a), a SAED pattern (b), and fast Fourier transform image (c) of Si QDs.

band centered at 2150 and 914  $\text{cm}^{-1}$  for the  $\nu(\text{Si-H})$  stretching vibration and  $\delta(\text{Si-H})$  bending vibration. Strong  $\nu(\text{Si-Si})$  stretching vibration appeared at

611  $\text{cm}^{-1}$ , indicating that the Si QDs consisted of only silicon and hydrogen atoms. Absolute quantum yields of blue and green luminescence were 5.8 and 5.6%, respectively. The detection of DMNB involves measurement of the quenching of photoluminescence of blue and green luminescent Si QDs by introducing  $1.11 \times 10^{-6}$  M,  $2.18 \times 10^{-6}$  M,  $3.21 \times 10^{-6}$  M,  $4.20 \times 10^{-6}$  M, and  $5.16 \times 10^{-6}$  M of DMNB, as seen in Fig. 2.3. The Stern. Volmer equation was used to quantify the differences in quenching efficiency for DMNB. The Stern.Volmer constant ( $K_{sv}$ ) is calculated using eqn (1).

$$\frac{I_f^0}{I_f} = 1 + K_{sv} \cdot [Q] \quad (1)$$

where  $I_f^0$  is the intensity without a quencher,  $I_f$  is the intensity with a quencher, and  $[Q]$  is the concentration of the quencher. The Stern.Volmer plot is depicted in Fig. 2.4. A linear Stern. Volmer relationship is observed in both cases. Stern.Volmer constants for blue and green luminescent Si QDs were 25 900 and 21 300, respectively. It can be observed that blue luminescent Si QDs ( $\lambda_{\text{max}} = 460$  nm) have a higher quenching efficiency than green luminescent Si QDs ( $\lambda_{\text{max}} = 520$  nm). This might be caused by the wider band gap energy of blue luminescent Si QDs. To avoid the possibility of quenching behavior derived from a molecular impurity generated during the synthesis, ethylenediamine was added to the blue luminescent Si QDs in solution which showed no significant changes in the PL spectra. A linear Stern.Volmer relationship may be observed if either a static or dynamic quenching process is dominant. The lifetime ( $\tau$ ) of blue luminescent Si and CdSe QDs has been measured. Lifetimes of CdSe and silicon quantum dots were 36.81 and 3.76 ns, respectively.

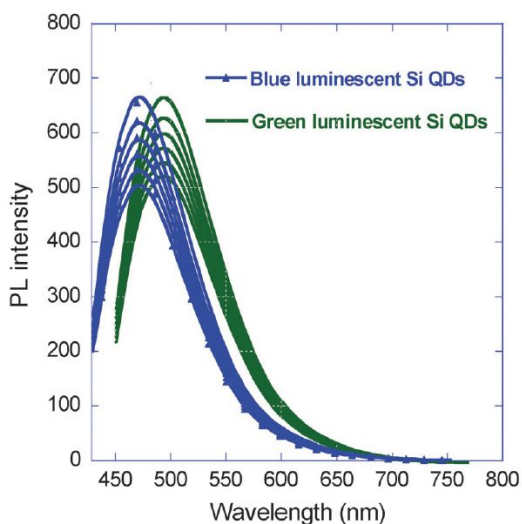


Figure. 2.3 PL quenching spectra of Si QDs recorded upon every addition of  $1.11 \times 10^{-6}$ ,  $2.18 \times 10^{-6}$  M,  $3.21 \times 10^{-6}$  M,  $4.20 \times 10^{-6}$  M, and  $5.16 \times 10^{-6}$  M of DMNB at each  $\lambda_{\text{max}} = 460$  nm (blue) and  $\lambda_{\text{max}} = 520$  nm (green) of Si QDs.

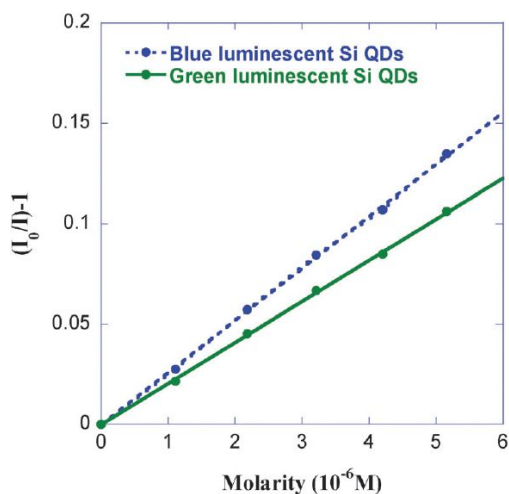


Figure. 2.4 The Stern-Volmer plots for quenching efficiency of the blue and green photoluminescent Si QDs with the introduction of DMNB.

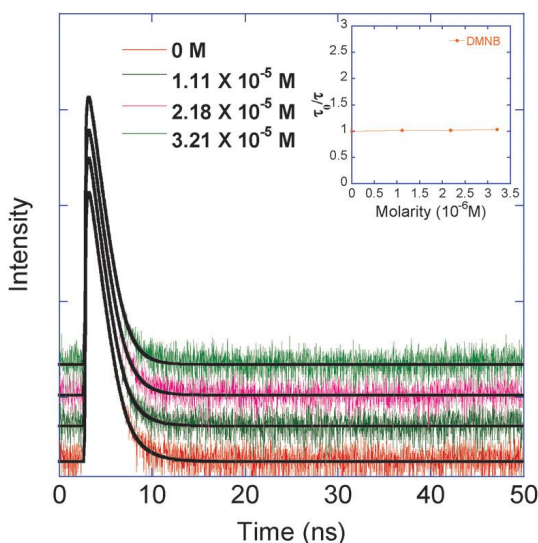


Figure. 2.5 Fluorescence decays of blue luminescent Si QDs for different concentrations of DMNB; the plots of fluorescence lifetime ( $\tau_0/\tau$ ), shown in the inset, are independent of the added DNMB.

The fluorescence lifetimes as a function of DNMB concentration were also measured and are shown in Fig. 2.5. No change in the mean lifetime was observed upon adding DNMB, indicating that the static quenching process is dominant for Si QDs. To compare with other QDs for sensing DMNB, we synthesized cadmium selenide (CdSe) QDs by following De Mello Donega'et al.'s method.[28] Blue ( $\lambda_{\text{max}} = 460 \text{ nm}$ ) and green ( $\lambda_{\text{max}} = 525 \text{ nm}$ ) luminescent CdSe QDs were selected to match the peak wavelengths of Si QDs. Again by utilizing blue and green luminescent CdSe QDs, the DMNB sensing experiment was carried out in the same fashion as that when using Si QDs. However the results were quite contrary as seen in Fig. 2.6. Introduction of  $1.11 \times 10^{-6} \text{ M}$ ,  $2.18 \times 10^{-6} \text{ M}$ ,  $3.21 \times 10^{-6} \text{ M}$ ,  $4.20 \times 10^{-6} \text{ M}$ , and  $5.16 \times 10^{-6} \text{ M}$  of DMNB had no effect on both blue and green PL spectra of CdSe QDs. Since quenching of PL is the result of electron

transfer, the relatively high lying LUMO energy level of DMNB might have prevented accepting electrons from CdSe QDs.

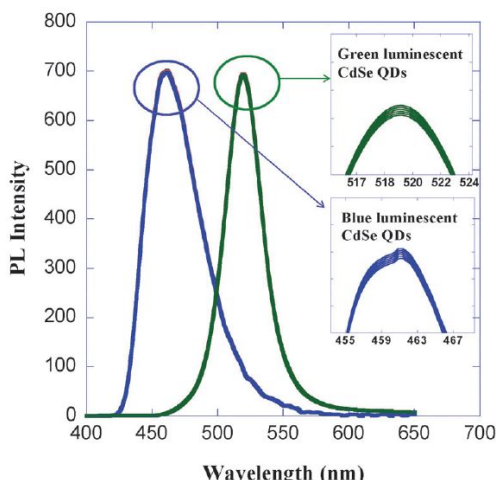


Figure. 2.6 Quenching of photoluminescence spectra of the blue (blue) and green (green) luminescent CdSe QDs with addition of  $1.11 \times 10^{-6}$  M,  $2.18 \times 10^{-6}$  M,  $3.21 \times 10^{-6}$  M,  $4.20 \times 10^{-6}$  M, and  $5.16 \times 10^{-6}$  M of DMNB.

QDs may be required to have a higher lying conduction band for an easier and effective electron transfer to analytes that have high lying LUMO energy levels. Qualitative bands of Si QDs and CdSe QDs, depicted in Fig. 2.7, explained the possible state of energy bandgaps. This suggested that the higher lying conduction band edge of Si QDs accommodated a photo-induced electron transfer which caused quenching of PL of Si QDs. On the other hand, photo-induced electron transfer quenching was not feasible by CdSe QDs, due to their lower lying conduction band edge. A high conduction band edge of a sensory material might be the key factor when detecting electron deficient analytes with high lying LUMO energy levels.

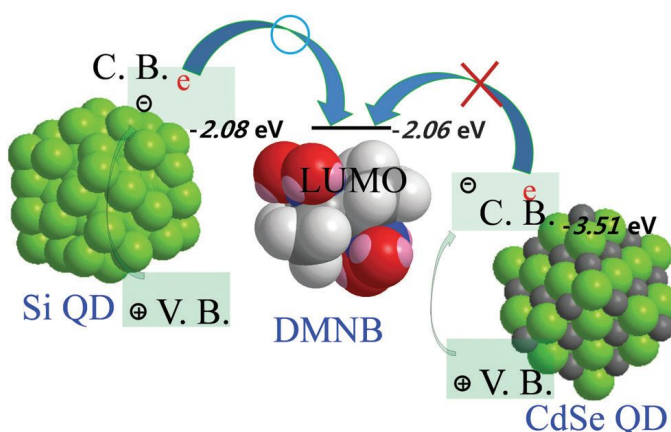


Figure. 2.7 Qualitative band diagram of Si QDs (left) and CdSe QDs (right) illustrated for sensitivity to DMNB. CB band edge level for Si QDs was optimized at the 6-31G\* level, with the final energy also calculated at the 6-31G\* level.[29] LUMO of DMNB was determined by theoretical calculations at the B3LYP/6-31G\* level of theory.[30] CB band edge value for CdSe QD was directly taken from research by Querner et al.[31]

There have been a number of reports on fluorescence-based sensing of DMNB by numerous compounds. One of them was (salophen) Zn which showed a Stern-Volmer Constant  $K_{sv}$  of 2.1[12] Other compounds such as a dendrimer incorporated thiophene attached to a triphenyl amine center and a carbazole dendrimer showed Stern-Volmer Constant  $K_{sv}$  of approximately 20 and 40, respectively.[32,33] (Salophen) Zn, a dendrimer incorporated thiophene attached to a triphenyl amine center, and a carbazole dendrimer had PL QYs of 30 to 60%, 40 to 75%, and 18 to 65%, respectively, which are significantly higher than that of Si QDs. Additionally, the PL QYs of blue and green luminescent CdSe QDs were 30.8% and 30.6%, respectively. This suggested that the PL QY plays very little or no role in fluorescence-based sensing of DMNB, since the PL quenching efficiency of Si QDs was

about 5000 fold higher than that of other compounds mentioned above. It is worth noting that the detection efficiency by Stern-Volmer constants for DMNB is the highest compared to previously reported values.



## 2.4 Conclusions

To summarize, Si QDs obtained by the reaction of magnesium silicide with ethylenediamine dihydrochloride from our previous study were utilized to explore a possibility of detecting an explosive taggant as well as to understand the sensing mechanism. Two different emission bands of Si QDs were synthesized at a peak wavelength of  $\lambda_{\text{max}} = 460$  (blue) and  $\lambda_{\text{max}} = 520$  nm (green). DNMB was successfully detected using blue luminescent Si QD solution with comparably good sensitivity, and analyzed by the Stern-Volmer relationship. The comparison result showed that Si QDs with a high lying conduction band have better sensitivity in sensing DNMB compared to CdSe QDs. For an easy electron transfer, the sensory system requires to have a matching conduction band edge with the LUMO energy level of the analyte.

## 2.5 References

- [1] D. Tyler McQuade, A. E. Pullen and T. M. Swager, *Chem. Rev.* 100, 2537-2574, 2000.
- [2] A. Lan, K. Li, H. Wu, D. H. Olson, T. J. Emge, W. Ki, M. Hong and J. Li, *Angew. Chem., Int. Ed. Engl.* 48, 2334-2338, 2009.
- [3] J.-S. Yang and T. M. Swager, *J. Am. Chem. Soc.*, 120, 5321-5322, 1998.
- [4] J.-S. Yang and T.M. Swager, *J. Am. Chem. Soc.*, 120, 11864-11873, 1998.
- [5] H. Sohn, R. M. Calhoun, M. J. Sailor and W. C. Trogler, *Angew. Chem.* 113, 2162-2163, 2001.
- [6] H. Sohn, M. J. Sailor, D. Magde and W. C. Trogler, *J. Am. Chem. Soc.* 125, 3821-3830, 2003.
- [7] S. W. Thomas III, J. P. Amara, R. E. Bjork and T. M. Swager, *Chem. Commun*, 4572-4574, 2005.
- [8] A. W. Czarnik, *Nature*, 394, 417-418, 1998.
- [9] D. S. Moore, *Rev. Sci. Instrum.* 75, 2499-2512, 2004.
- [10] R. G. Ewing and C. J. Miller, *Field Anal. Chem. Technol.* 5, 215-221, 2001.

- [11] S. Pramanik, C. Zheng, X. Zhang, T. J. Emge and J. Li, J. Am. Chem. Soc. 133, 4153-4155, 2011.
- [12] M. E. Germain, T. R. Vargo, P. G. Khalifah and M. J. Knapp, Inorg. Chem., 46, 4422-4429, 2007.
- [13] V. S. Lin, K. Motesharei, K. S. Dancil, M. J. Sailor and M. R. Ghadiri, Science, 3791, 840-843, 1997.
- [14] J.-H. Park, L. Gu, G. von Maltzahn, E. Ruoslahti, S. N. Bhatia and M. J. Sailor, Nat. Mater, 8, 331-336, 2009.
- [15] E. J. Anglin, L. Cheng, W. R. Freeman and M. J. Sailor, Adv. Drug Delivery Rev. 60, 1266-1277, 2008.
- [16] H. Sohn, S. Le'tant, M. J. Sailor and W. C. Trogler, J. Am. Chem. Soc. 122, 5399-5400, 2000.
- [17] C. B. Murray, D. Norris and M. G. Bawendi, J. Am. Chem. Soc. 115, 8706-8715, 1993.
- [18] J. E. B. Katari, V. L. Colvin and A. P. Alivisatos, J. Phys. Chem., 98, 4109-4117, 1994.
- [19] C. P. Collier, Science, 277, 1978-1981, 1997.
- [20] V. L. Colvin, M. C. Schlamp and A. P. Alivisatos, Nature, 370,

354-357, 1994.

[21] W. C. W. Chan and S. Nie, *Science*, 281, 2016-2018, 1998.

[22] C. S. Yang, R. A. Bley, S. M. Kauzlarich, H. W. H. Lee and G. R. Delgado, *J. Am. Chem. Soc.* 121, 5191-5195, 1999.

[23] D. Neiner, H. W. Chiu and S. M. Kauzlarich, *J. Am. Chem. Soc.* 128, 11016-11017, 2006.

[24] R. K. Baldwin, K. A. Pettigrew, J. C. Garono, P. P. Power, G. Y. Liu and S. M. Kauzlarich, *J. Am. Chem. Soc.* 124, 1150-1151, 2002.

[25] J.-K. Choi, S. Jang, H. Sohn and H.-D. Jeong, *J. Am. Chem. Soc.*, 131, 17894-17900, 2009.

[26] B. Cho, S. G. Lee, H. G. Woo and H. Sohn, *J. Nanosci. Nanotechnol.*, 13, 384-387, 2013.

[27] B. Cho, S. Baek, H.-G. Woo and H. Sohn, *J. Nanosci. Nanotechnol.*, 14, 5868-5872, 2014.

[28] C. De Mello Donega', S. G. Hickey, S. F. Wuister, D. Vanmaekelbergh and A. Meijerink, *J. Phys. Chem. B*, 107, 489-496, 2003.

[29] Z. Zhou, R. A. Friesner and L. Brus, *J. Am. Chem. Soc.*, 125, 15599-15607, 2003.

[30] J. C. Sanchez, A. G. DiPasquale, A. L. Rheingold and W. C. Trogler, Chem. Mater. 19, 6459-6470, 2007.

[31] C. Querner, P. Reiss, S. Sadki, M. Zagorska and A. Pron, Phys. Chem. Chem. Phys. 7, 3204-3209, 2005.

[32] D. A. Olley, E. J. Wren, G. Vamvounis, M. J. Fernee, X. Wang, P. L. Burn, P. Meredith and P. E. Shaw, Chem. Mater. 23, 2011, 789-794.

[33] G. Tang, S. S. Y. Chen, P. E. Shaw, K. Hegedus, X. Wang, P. L. Burn and P. Meredith, Polym. Chem., 2, 2360, 2011.

# Appendices

# Appendix

## Curriculum Vitae

---

### Educations (학위)

- Ph. D.** 2011. 02. ~ 2017. 02. Chemistry, Chosun University  
Research Advisor : **Prof. Honglae Sohn**  
Thesis Title : “**Nanosensor Research Based on Porous Silicon Photonic Crystals and Silicon Quantum Dots**”
- M. S.** 2009. 03. ~ 2011. 02. Chemistry, Chosun University  
Research Advisor : **Prof. Honglae Sohn**  
Thesis Title : “**Investigation of Photoluminescence Efficiency of n-Type Porous Silicon by Controlling of an Etching Time and Applied Current Densities**”
- B. S.** 2002. 03. ~ 2009. 02. Chemistry, Chosun University

### Publications (논문게재)

#### SCI Journals (국제전문학술지)

1. “Fabrication of Gradient Optical Filter Containing Anisotropic Bragg Nanostructure.”, B. Cho, S. Um, H.-G. Woo, H. Sohn\*, Journal of Nanoscience and Nanotechnology, 2011, 11, 7163-7166
2. Multi-spot Porous Silicon Chip Prepared from Asymmetric Electrochemical Etching for Human Immunoglobulin G Sensor.”, S. Um, B. Cho, H.-G. Woo, H. Sohn\*, Journal of Nanoscience and Nanotechnology, 2011, 11, 7061-7064
3. Porous-silicon photonic-crystal platform for the rapid detection of

- nano-sized superparamagnetic beads for biosensing applications”, P. J. Ko, R. Ishikawa, T. Takamura, Y. Morimoto, B. Cho, H. Sohn, A. Sandhu, *Nanoscience and Nanotechnology Letters*, 2011, 3 (5), 612-616.
4. Investigation of Photoluminescence Efficiency of n-Type Porous Silicon by Controlling of an Etching Time and Applied Current Densities”, B. Cho, S. Jin, B.-Y. Lee, M. Hwang, H.-C. Kim, .H. Sohn\*, *Microelectronic Engineering*, 2012, 89,92-96.
5. “Fabrication of Human IgG Sensors Based on Porous Silicon Interferometer Containing Bragg Structures”, B. Cho, B.-Y. Lee, H.-C. Kim, H.-G. Woo, H. Sohn\*, *Journal of Nanoscience and Nanotechnology*, 2012, 12, 4159-4162.
6. “Detection of Nerve Agent Simulants Based on Photoluminescent Porous Silicon Interferometer”, S. Kim, B. Cho, H. Sohn\*, *Nanoscale Research Letters*, 2012, 7, 527.
7. “Fabrication and Characterization of Photoluminescent Silicon Nanoparticles for Durg Delivery Applications”, J. Ryu, B. Cho, H.-G. Woo, S. Cho, H. Sohn\*, *Journal of Nanoscience and Nanotechnology*, 2013, 13, 157-160.
8. “Synthesis and Optical Characterization of Silicon Nanoparticles”, B. Cho, S.-G. Lee, H.-G. Woo, H. Sohn\*, *Journal of Nanoscience and Nanotechnology*, 2013, 13, 384-387.
9. “Anisotropic Multi-spot DBR Porous Silicon Chip for the Detection of Human Immunoglobulin G”, B. Cho, S. Um, H. Sohn\*, *Journal of Nanoscience and Nanotechnology*, 2014, 14, 4832-4836.
10. “Fabrication and Optical Characterization of Multi-Encoded Rugate Porous Silicon/Polymer Composite”, B. Cho, S.-G. Lee, H.-G. Woo, and H. Sohn\*, *Journal of Nanoscience and Nanotechnology*, 2014, 14, 5844-5848.



11. "Synthesis of Silicon Quantum Dots showing High Quantum Efficiency", B. Cho, S. Baek, H.-G. Woo, and H. Sohn\*, Journal of Nanoscience and Nanotechnology, 2014, 14, 5868-5872.
12. "Detection of organic vapors based on photoluminescent bragg-reflective porous silicon interferometer", J. Ahn, B. Cho, S. Kim and H. Sohn\*, Journal of Nanoscience and Nanotechnology, 2015, 15, 4999-5003.
13. "Detection of human Ig G using photoluminescent porous silicon interferometer", B. Cho, S. Kim, H.-G. Woo and H. Sohn\*, Journal of Nanoscience and Nanotechnology, 2015, 15, 1083-1087.
14. "Synthesis and characterization of microwave-exfoliated grapheme oxide-wrapped silicon nanowire via hydrosilylation", D. Shin, B. Cho, J. Ahn, S. Kim, K. Y-C and H. Sohn\*, Journal of Nanoscience and Nanotechnology, 2015, 15, 1748-1751.
15. "Silicon quantum dot sensors for an explosive taggant, 2,3-dimethyl-2,3-dinitrobutane(DMNB)", J.-S. K<sup>†a</sup>, B. Cho<sup>‡b</sup>, S.-G. Cho and H. Sohn\*, Chemical Communications, 2016, 52 (53), 8171-8322.  
(<sup>‡</sup> These authors contributed equally to this work.)

#### Domestic Journals (국내전문학술지)

1. "Photoluminescent Porous Silicon for TNT Vapor Sensor", S.-K. Kim, B. Cho, S.-G. Cho and H. Sohn\*, Journal of the Chosun Natural Science, 2016, 7 (1), 1-3.
2. "Preparation and Optical Characterization of DBR/Host Dual Porous Silicon Containing DBR and Host Structures", T.-E. Choi, J. Yang, S. Um, S. Jin, B. Cho, S. Cho and H. Sohn\*, Journal of the Chosun Natural Science, 2010, 3, 78-83.

- “Detection of Volatile Alcohol Vapors Using Silicon Quantum Dots Based on Porous Silicon”, B. Cho, S. Um, S. Jin, T.-E. Choi, J. Yang, S. Cho and H. Sohn\*, Journal of the Chosun Natural Science, 2010, 3, 117-121.
4. “Synthesis and Optical Characterization of 2,5-Difunctional Siloles”, T.-E. Choi, J. Yang, J. Han, S. Um, S. Jin, B. Cho, and S. Cho, Journal of the Chosun Natural Science, 2009, 2, 50-53.

## Awards (수상)

1. 제3회 한국실리콘학회 우수포스터 발표상 (2014. 02. 13)  
“Synthseis Phenyl-Vinyl-Based Polysiloxane Resins by Using Oligohydrosiloxanes”
2. 제 4회 한국실리콘학회 우수포스터 발표상 (2015. 02. 12)  
“Investigation of Photoluminescence Efficiency of Silole-Capped Silicon Quantum Dots Based for Sensing Applications ”
3. 제18회 대한화학회 광주 전남 전북지부 학회 우수 포스터 발표상 (2016. 05.27)  
“ High Luminescent and Size-tunable Silicon Quantum Dots and their application for Sensing Explosives”

## Project Activity (국책 연구 수행 경력)

1. "실리콘 화합물 이용한 고안정성 에너지 저장장치용 전해질 개발"  
(한국학술진흥원, 2016.07.01~2016.12.31)-참여연구원
2. "폭발물 탐지용 Bragg 적층 반도체칩 센서 플랫폼 개발"  
(국방과학연구소 : 국제공동연구사업, 2015.10.14~2016.12.31)  
-실무담당자
3. "Iptycene 구조를 갖는 Silafluorene 유도체의 합성방법 개발과 이들을

이용한 응용연구"

(한국연구재단: 일반연구지원사업, 2013.11.01~2016.10.31)-실무담당자

4. "초고강도 폭발물 감지용 실리콘 양자점에 관한 연구"

(국방과학연구소 : 순수기초사업, 2013.09.15~2015.12.15)-실무담당자

5. "고굴절 고투명 유/무기-실록산 하이브리머 LED 봉지재 개발"

(한국연구재단: 지역혁신인력양성사업, 2012.05.01~2015.04.30)-실무담당자

6. "실리콘양자점의 새로운 합성방법의 개발 및 응용에 대한 연구"

(한국연구재단: 일반연구지원사업, 2010.05.01~2013.04.30)-실무담당자

### Patents (특허 출원 및 등록)

1. "광발광성 실리콘나노입자를 이용한 약물전달체계 및 그의 제조방법"

B.Cho. 2013-0006444, 2013/01/21-한국특허 출원

(조선대학교 산학협력단)

2. "카드뮴 셀레나이드 양자점을 이용한 폭발물 탐지용 화학센서"

B.Cho. 20xx-xxxxxxx, 201x/xx/xx-한국특허 출원 (국방과학연구소)

3. "실리콘양자점을 이용한 폭발물 탐지용 화학센서"

B.Cho. 20xx-xxxxxxx, 201x/xx/xx-한국특허 출원 (국방과학연구소)